Compositional Engineering of Perovskite Absorber Material to Enhance the Stability of PSCs

By

Tanzeela Yousaf

Reg # 00000273763
Session 2018-2022

Supervised by
Dr. Nadia Shahzad

Co-Supervised by

Dr. Zuhair S. Khan

A Thesis Submitted to the US-Pakistan Center for Advanced Studies in Energy in partial fulfillment of the requirements for the degree of

MASTER of SCIENCE

in

ENERGY SYSTEMS ENGINEERING

US-Pakistan Center for Advanced Studies in Energy (USPCAS-E)

National University of Sciences and Technology (NUST)

H-12, Islamabad 44000, Pakistan

June 2022

THESIS ACCEPTANCE CERTIFICATE

Certified that final copy of MS thesis written by **Miss Tanzeela Yousaf**, (Registration No. 00000273763), of U.S.-Pakistan Center for Advanced Studies in Energy, has been vetted by undersigned, found complete in all respects as per NUST Statues/Regulations, is within the similarity indices limit and is accepted as partial fulfillment for the award of MS degree. It is further certified that necessary amendments as pointed out by GEC members of the scholar have also been incorporated in the said thesis.

Signature: ______________________________

Name of Supervisor Dr. Nadia Shahzad

Date: ________________________

Signature (HoD): ________________________

Date:

Signature (Dean/Principal): __________________

Date: ____________________________________

CERTIFICATE

This is to certify that work in this thesis has been carried out by **Miss Tanzeela Yousaf** and completed under my supervision in Energy Systems Engineering Laboratory, US-Pakistan Center for Advanced Studies in Energy (USPCAS-E), National University of Sciences and Technology, H-12, Islamabad, Pakistan.

Supervisor: ______________

Dr. Nadia Shahzad
USPCAS-E, NUST H-12, Islamabad

Co-Supervisor: ______________

Dr. Zuhair S. Khan
USPCAS-E, NUST H-12, Islamabad

GEC member # 1: ______________

Dr. Sofia Javed
USPCAS-E, NUST H-12, Islamabad

GEC member # 2: ______________

Dr. Muhammad Imran Shahzad
NCP, QAU, Islamabad

HoD- ESE ________________

Dr. Rabia Liaquat
USPCAS-E, NUST H-12, Islamabad

Principal/ Dean ______________

Prof. Dr. Adeel Waqas
USPCAS-E, NUST H-12, Islamabad

Acknowledgments

All praises and thanks are for the **Almighty Allah**, the Merciful, the only creator of the universe and source of all knowledge and wisdom, who blessed me with health, thoughts, and talented teachers, helped friends, and afforded opportunity to complete this study. I offer my humblest thanks to the **Holy Prophet Hazrat Muhammad (Peace be Upon Him)**, whose moral and spiritual teachings enlightened my heart and mind, and flourished my thoughts towards achieving high ideals of life.

I feel much honored to express my deepest sense of gratitude and indebtedness to my honorable supervisor**, Dr. Nadia Shahzad**, from the core of my heart for his dynamic supervision and indefatigable assistance at all time during the entire study program and in the preparation of this manuscript. I am thankful to my Co- Supervisor **Dr. Zuhair S. Khan** for his guidance and support in completing my MS thesis. I am thankful to my GEC members **Dr. Sofia Javed** and **Dr. M. Imran Shahzad** for their collaboration, keen interest, and effective guidance that helped me to complete the challenging work of my MS thesis. I would also like to pay my special thanks to HoD ESE **Dr. Rabia Liaquat** for her motivation and support to do something extraordinary during the research and also in the future.

Here I would be very selfish if I do not express my sincere and special gratitude to my loving **parents** who had always wished to see me glittering high on the skies of success whose endless efforts and best wishes sustained me at all stages of my life. I also want to thank my dearest **Siblings** my loving **Sister Amina Yousaf and Zainab Choudhary** for their inspiring encouragement and moral support. **Friends** especially thanks to **Tahreem Asad Khan** because of her unforgettable company are the golden memories of my life. Heart-full thanks to my **all-lab friends** especially **Naveed Hussain, Ahad Hussain Javed, Abdul Star, and Ali Tariq** for providing their expert advice and positive company during my study.May **ALLAH** give them good health and long happy life. There are many people whose names are not mentioned here and I wish to express my gratitude to all of them for making this project a very good experience for me. May Allah bestow strength and contentment to all these splendid celebrities (Ameen).

Regards,

Tanzeela Yousaf

Dedication

*To **Almighty Allah**, for his daily blessings,*

make all my work possible.

*To my **parents** who are full of sympathy and*

everlasting love.

*To **Dr. Nadia Shahzad**; for her Kind*

behavior and inspiring guidance.

To my dearest homeland, Pakistan

Abstract

The development of organometal halide-based perovskites solar cells (PSCs) has made remarkable progress in the photovoltaic technology field. The commercialization of PSCs is being rendered owing to its poor stability and higher material cost for hole transport layer (HTL) and electrodes. To counter these issues carbon-based HTL and noble-metal-free PSCs are being used. In this work, we systematically studied the effect of Cs-doping on perovskite film morphology and device performance. The results showed that when Cs-doping concentration was in the range of 9%, there was a substantial change in the optoelectronic and morphological properties of perovskite film. The grain size was improved from 70nm (undoped film) to 170nm (9% Cs-doped film) with a reduction in the grain boundaries. The device fabrication was carried out in a dry glove box at 10% relative humidity by using carbon as a counter electrode (CE). Consequently, Cs-doping with carbon CE improved the hydrophobicity and non-radiative charge recombination at the surface of the carbon/perovskite film interface. The efficiency of the devices was improved to 5.27% at a 9% Cs-doping level as compared to the 0% Cs-doping with 1.55% efficiency. Moreover, this technique will reduce the fabrication costs of PSCs significantly promising a sustainable future for this technology.

Keywords: Perovskite Solar Cells, Carbon counter electrode, HTL, Hydrophobic

Table of Contents

List of Figures

List of Tables

Publications

1. **Tanzeela Yousaf,** Abdul Satar, Mohammad Ali Tariq, Naveed Hussain, Zuhair. S. Khan. Sofia Javed, Mohammad Imran Shahzad **"Fabrication of Cs-doped carbon-based perovskite solar cells in the ambient environment”** Journal of Solid Thin Films **(Status: Under Review)**

2. Naveed Hussain, Nadia Shahzad, **Tanzeela Yousaf**, Ahad Hussain Javed, Sheheryar Khan, Adeel Waqas, Rabia Liaqat**. “Designing of Homemade Soiling Station to Explore Soiling Loss Effects on PV Modules”.** Solar Energy Journal of Elsevier. **(Status: Published)**

3. Naveed Hussain, Nadia Shahzad, **Tanzeela Yousaf,** Ahad Hussain Javed, **“Study of soiling effects on PV module Performance at different environmental parameters using Homemade soiling station”** Journal of Sustainable Technology and Energy Assessment **(Status: Published)**

4. Abdul Satar, Nadia Shahzad, Mohammad Ali Tariq, **Tanzeela Yousaf,** Muhammad Salik Qureshi, Muhammad Imran Shahzad, Rabia Liaquat, Majid Ali, **“Carbonyl functional group assisted crystallization of mixed tin-lead narrow bandgap perovskite absorber in ambient conditions”** Journal of Applied Physics Letters **(Status: Under Review)**

5. Mohammad Ali Tariq, Nadia Shahzad, Abdul Satar, **Tanzeela Yousaf,** Ahad Hussain Javed, Naseem Iqbal, Muhammad Imran Shahzad, **“Highly stable and efficient NH 3 (aq)/DES processed CuSCN bilayers for perovskite solar cells”,** Journal of Solar Energy and Materials. **(Status: Under Review)**

List of Abbreviations

Abbreviation	**Nomenclature**
PSCs	Perovskite Solar Cells
PCE	Power Conversion Efficiency
CE	Counter Electrode
LT	Low Temperature
HT	High Temperature
C-PSCs	Carbon-Based Perovskite Solar Cells
ETL	Electron Transport Layers
HTL	Hole Transport Layer
PVAc	Polyvinyl Acetate
FWHM	Full Width Half Maxima
FF	Fil Factor
V_{oc}	Open Circuit Voltage
I_{sc}	Short Circuit Current
Eu	Urbach Energy

Chapter 1

Introduction

1.1 Energy Crisis and Climate Change

Industrial and economic development gives rise to the energy demand. As a result of increased energy demand use of fossil fuels increased to meet with requirements of the newly industrialized world which causes adverse effects on our environment and gives rise to its prices. Industries being a major emitter of CO_2 as a result of fossil fuels usage is the most challenging problem [1,2]

In response to these problems and as a method of fostering a more sustainable future, a new energy market is emerging[3]. This new energy economy includes renewable energy sources like solar, wind, hydroelectric, biogas, biomass, bioenergy, geothermal, and tidal energy. Due to its availability and clean energy source, solar energy is amongst the most well-known forms of energy. One of the most plentiful energy sources is solar, and even a small amount of conversion may help us meet our energy demands and combat the issue of rising energy prices and demand.

1.2 Solar Energy Potential

Global solar total capacity was 714 GW at the end of 2020 [4]. We receive 164 watts of sun's electricity on average per square meter of surface area, which is fantastic. To power, the entire world with solar energy, a powerful table light (150 watts) could be placed on every square meter of the planet. That is to say, if solar panels covered just 1% of the Sahara, there would be enough energy to power the entire planet. It is capable of producing solar energy.

In 2018, primary energy consumption increased by 2.9 percent, nearly double the 10-year average which was 1.5 percent. Carbon emissions increased by 2.0 percent, while the annual average price of fuel oil increased by 2.0 percent to \$71.31/barrel, from \$54.19/barrel in 2017. On average, 1.4 million barrels of oil are produced per day [5].

On the other hand, all commercially available renewable technology costs decreased in 2018. According to figure 1.1, the average cost of concentrated solar power has dropped by 26%, biofuels by 14%, solar PV and coastal wind both by 13%, hydroelectric by 12%, and geothermal and offshore wind both by 1%. Onshore wind and solar PV power are less expensive than fossil fuels[6].

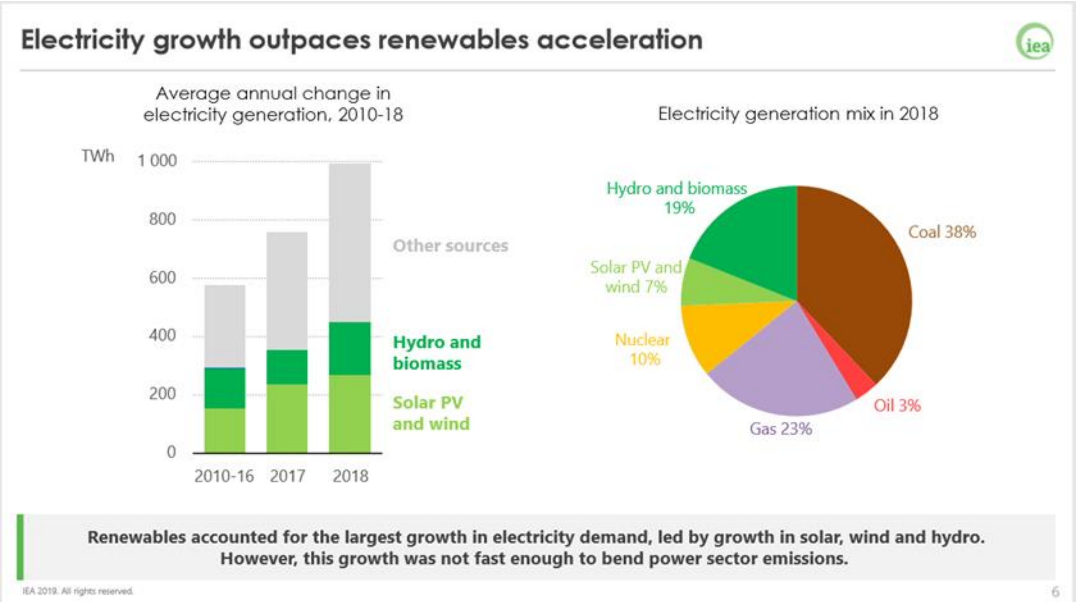
Electricity growth outpaces renewables acceleration

Renewables accounted for the largest growth in electricity demand, led by growth in solar, wind and hydro. However, this growth was not fast enough to bend power sector emissions.

Figure 1.1: Average annual change in electricity generation 2010-2018 [7]

There is a drawback, though. The sun's energy travels from space to the earth as a combination of heat and light. Light cannot turn on a TV or a vehicle using direct sunlight or heat, but it does cause plants to grow, produce food, and keep themselves warm enough to thrive. We must discover a way to convert solar energy into more practical kinds of energy, like electricity. Exactly that is what solar cells achieve [8].

In recent decades, this steady drop and low-cost decarbonization have aroused researchers' attention. Due to the increasing energy demand and the depletion of fossil fuels, substantial efforts are being undertaken to increase the use of alternative energy sources in the future.

1.3 Pakistan’s Solar Potential

Renewable energy development and effective use are growing in Pakistan. Pakistan is one of those countries where the sun shines almost all the year and has a significant solar power-producing potential. Average solar radiation throughout the country remains 136.05W/m^2 to 287.36W/m^2. More of the period year sun shines for 10 hours a day which could result in 45-83MW power per month from just a 100m^2 area. The strength of solar radiation is constant across the nation from March to October. The radiation intensity in Sindh continues above 200 W/m2 from February to October, from March to October in Baluchistan, from April to September in the NWFP, the Northern areas, and the Kashmir region, and from March to October in Punjab. The majority of southern Punjab, Sindh, and Baluchistan has a great potential for solar energy throughout the year. In the southern part of Pakistan, the yearly sun's direct solar irradiance is greater than 5kWh/m2/day, which is perfect for solar technologies[9].

1.4 Solar energy technologies

There are three major types of solar energy:

- Solar thermal
- Concentrating solar power
- Solar Photovoltaics

Each of these converts the sunlight into a form of energy that we can store for industrial, domestic, and commercial use.

1.4.1 Solar Thermal

Solar thermal energy uses sunlight for heating and cooling purposes. Thermal energy is for water heating, space heating, and even cooling spaces. The heat from solar radiation heats the water which can be stored for later use or transferred to pipes for space heating. This technology can cut done on electricity and gas consumption in the winters.

1.4.2 Concentrating Solar Power

Concentrating solar power or CSP for short is mostly used for industrial purposes because of the large scale of the power plant. The technology employs mirrors for reflecting the sunlight and directing it towards a receiver that collects it in the form of heat. This heat can latent be used to produce electricity.

1.4.3 Solar PV

Solar photovoltaic energy is created directly from sunlight using semiconductors. When solar radiation falls on a solar PV cell, the semiconductor frees electrons to generate an electric current. Solar PV technology involves the use of solar cells which are connected in series and mounted on a module. Multiple modules can be arranged from an array that makes up a solar panel. The number of arrays can be changed according to the amount of solar power required.

1.4.3.1 Working of a Solar PV cell

Solar technology is a form of electronic device that quickly converts sunlight into power by absorbing it. Its oval shape, blue color, and size are comparable to an adult palm. A solar system is a larger apparatus that is typically created by combining many solar cells. Like other types of cells, solar cells are made to generate electricity. On the other side, solar panels use sunlight to produce power rather than chemicals. Because they produce energy from sunlight, they are also called solar cells (PV) ("photo" means light in Greek). Photons are the minuscule constituents of light. The sun's rays resemble a brilliant yellow fire of countless billions of photons in flight. The solar system collects these active particles from the road and transforms them into electrical currents or transitions. The solar collector's job is to transform the energy produced by several cells into a useable quantity of electricity and voltage, as shown in figure 1.2 because each cell produces various energy voltages. Today, silicon fragments (one of the most common soils and a chemical element found in sand) make up almost every solar cell, but there are other materials as we'll see. Additionally, there are other uses for it (or rather). Electricity is made available everywhere in the solar system when the sun shines on it because the solar cell's energy drives silicon electrons via an electric circuit[10].

1.4.3.2 Manufacturing of Solar Cells

Solar cell manufacturing Silicone is used in solar cells and transistor microchips (small switches). Silicone is a semiconductor, which is a type of material. It normally does not carry electricity, though it can do so in some instances. Solar cells are two layers of layers manufactured in a particularly treated form as a silicone dose that conducts energy in a certain wafer pattern. Because the underlying layer is narcotic, it has a few additional electrons. As positive silicon, this is referred to as type p. (because the electrons in this layer are negatively charged and small). The top layer produces a modest number of electrons and is in the opposite direction. Type n silicone is also known as negative silicone, shown in figure 1.2.

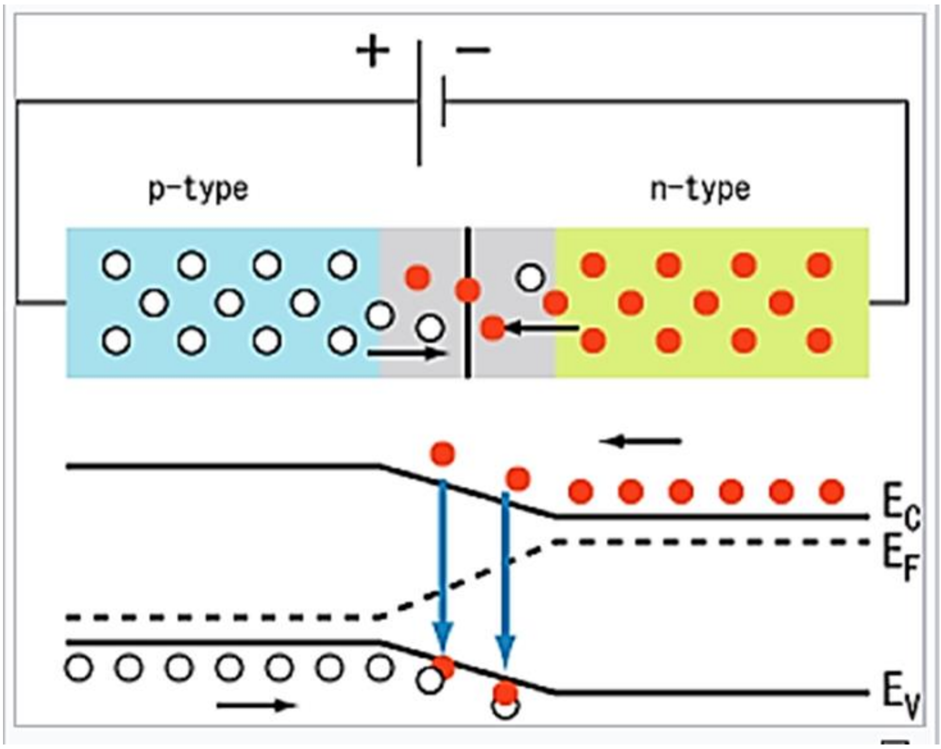

Figure 1.2: Schematic representation of PV junction[11]

The crossing of the two materials is prevented by applying the N-type silicone layer to the R-type silicone layer (the critical limit that these two types of silicone meet). When you connect this sandwich to the fire, the electrons can't reach the threshold, thus they don't flow. Light can be thought of as a stream of photons, which are active "light particles." Photons excite silicon atoms as they enter a sandwich. The incoming energy inflates the lower p-type layer's electrons, which then migrate to the circuit's top n-type layer and exit the cycle. The more electron jump, the stronger current is for brighter light. This is one of the so-called photovoltaic light, technically associated photoelectric effect, and it refers to solar energy (a trend that produces light)[10].

1.5 Different kinds of photovoltaic solar cells

Most solar panels currently mounted on roofs are silicone sandwiches that have been specially treated (or "doped") to increase electrical conductivity. To distinguish them from two other innovations, modern or second-generation and third-generation solar cells, scientists refer to these conventional solar cells as first-generation[11].

1.5.1 First Generation Solar Cells

Crystalline silicon wafers, also known as c-Si, are cut into large stems and cultivated for a month in extremely clean labs. These stems are used to make over 90% of the world's solar cells. Numerous crystals can be observed in the stem in addition to single monocrystalline or mono-Si crystals (polycrystalline, poly-Si, or poly-c-Si). The diagram in the figure illustrates the first generation of solar cells1.3.

Figure 1.3: 1st Generation Solar Cells[4]

1.5.2 Second Generation Solar Cells

The normal thickness of solar panels is less than one millimeter (about 200 micrometers, 200 meters, or more). However, these are full plates as opposed to second-generation thin-film solar cells (TPSC) or thin-film membranes (TFPV), which are over 100 times thinner (a few micrometers or a million meters deep). Some are made of different minerals, such as cadmium tellurium, even though the majority is still silicon (amorphous silicon, -Si, in which atoms are randomly placed rather than categorized in a continuous crystal structure). French diselenide and copper-iron-French diselenide (Cd-Te) (CIGS). Figure 1.4 illustrates the mounting of second-generation solar cells on windows, skylights, tiles, and a range of surfaces (support components), including metals, glass, and polymer (plastic)[4].

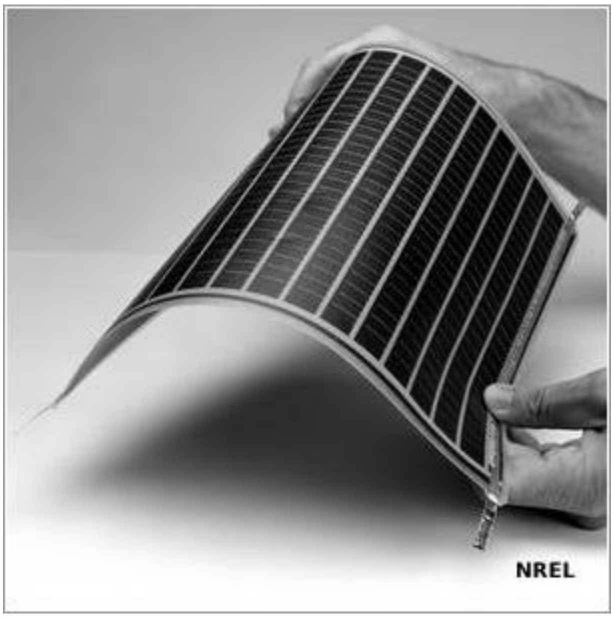

Figure 1.4: 2nd Generation solar Cell [4]

1.5.3 Third Generation Solar Cells

The most modern technique combines the best elements of cells from the first and second generations. Figure 1.5 illustrates their significant yields, which are comparable to those of first-generation cells (30% or more)[4].

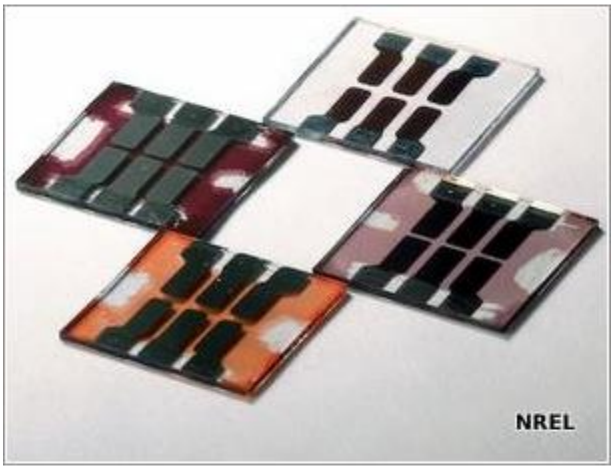

Figure 1.5: 3rd Generation Solar Cells [4]

Similar to second-generation components, they are made from materials other than "simple" silicon, like amorphous silicon, polymer materials (organic photovoltaic panels, OPV), perovskite crystals, and a range of other compounds (consisting of several layers of different semiconductor materials). Ideally, it should be more affordable, superior, and useful than the first or second generation [4].

1.6 The efficiency of solar cells

A fundamental tenet of physics is the law of energy conservation, which holds that energy cannot be created or destroyed but can only be transferred from one form to another. As a result, the energy produced by solar cells cannot outweigh the energy that sunlight impinges on them. We shall see that in practice they usually convert between 10% and 20% of the energy they acquire into electrical energy. The Shockley-Queisser limit, or potential limit efficiency of a single silicon solar cell, is around 30%, shown in figure 1.6.

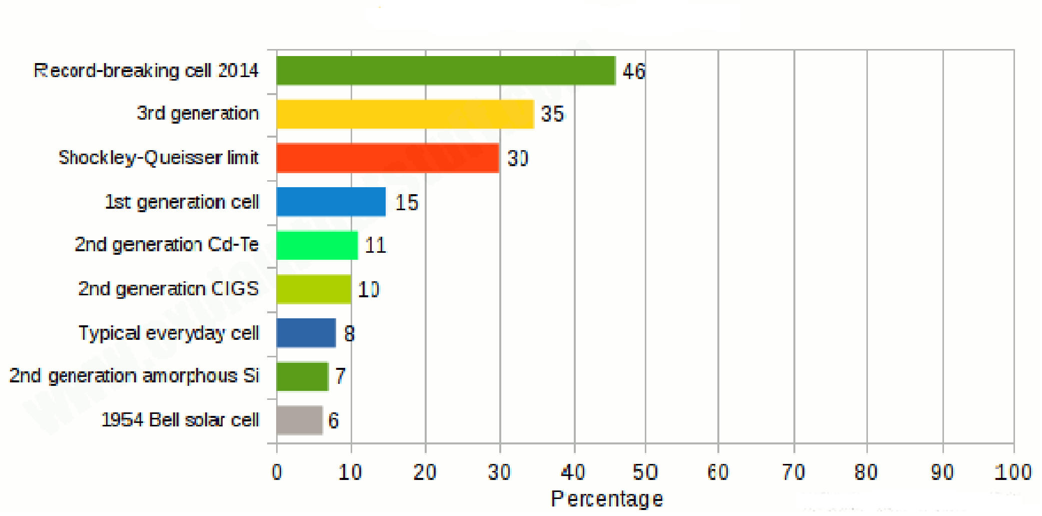

Figure 1.6: Efficiencies of different types and generations of solar cells [8]

Under ideal circumstances, the high-tech cells in the lab can manage an efficiency of 46% by using multiple junctions to collect photons of different energies. In the real world, household solar panels have an efficiency of about 15%, occasionally add a few percentage points, and are not likely to get any better. The very first single-cell solar interface is only 46% efficient in the lab, falling short of the Shockley-Queisser constraint's 30% efficiency. The panels' structure, placement, and spacing, even when they are in the shade, how clean you maintain them, how hot they are, and whether or not they are ventilated to keep cool are all actual economic issues that affect nominal efficiency.

1.7 Limitations of the previous generations

First-generation includes silicon-based solar cells and even though they offer a high efficiency the silicon is not affordable. Moreover, the fabrication process is complex and there are high costs associated with the materials. There are also many loss mechanisms associated with the first generation: (i) the photons have energy greater than the cell bandgap so energy is lost and dissipated as heat and (ii) the fermi level is lower for both p-type and n-type material is confined to the bandgap of silicon so the open circuit voltage is minimizing.

The basis of the second generation is thin-film technology and it is lower in cost than the first generation and cells have a higher absorption coefficient. However, their fabrication processes are susceptible to environmental contamination and the materials are not easily accessible. The third generation of solar cells addresses these issues with readily available materials, a greater theoretical efficiency limit, and simple fabrication techniques.

1.8 Research Problem

Perovskite solar cells (PSCs) have come forth as a viable option promising high photovoltaic efficiency and ultracheap energy solution aiming to prevail over crystalline silicon-based solar photovoltaic technology [3]. Meanwhile, single-junction PSCs are approaching their Shockley-Quiesser (SQ) efficiency limit, with a recently achieved new high of 25.8% efficiency and when used in tandem with another solar cell, they can cross the theoretical efficiency limit. Perovskite-based tandem solar cells (PSCs) are offering an exciting opportunity to break the SQ limit of single-junction PSCs. Normally, a tandem architecture involves two or more solar cells stacked one above the other, comprising an overlying wide bandgap (1.4-2.4 eV) sub cell acting as a front or top cell and an underlying low bandgap (1.2-1.3 eV) sub cell acting as a rear or bottom cell. The wide-bandgap perovskites solar cells are the most popular choice for multi-junction tandem architectures. Nevertheless, despite their higher efficiencies and lower fabrication costs, PSCs' large-scale manufacturing is hampered by several challenges, i.e., stability. PSCs degradation is influenced by several environmental factors, including visible and ultra violet light exposure, temperature effect, humidity, oxygen, and electrical bias. This proposed study aims to develop the perovskite absorber materials with compositional engineering to enhance the stability of existing PSCs by controlling the morphology, grain size boundaries, grain size, charge recombination, trap defect states, and hysteresis.

1.9 The objectives of the Research

- Compositional engineering of perovskite film with CsBr to enhance the stability of the perovskite solar cells.
- Synthesis of wide band gap perovskite film for the tandem application.
- Deposition of the Perovskite film at various CsBr doping concentrations in the ambient conditions.
- Fabrication of the whole device with carbon as a counter electrode.

- Characterized the morphological, optical, and structural properties of the perovskite film and electrical properties of the perovskite solar cells.

1.10 Thesis outlines

1. Chapter 2 describes the literature review related to compositional engineering perovskite solar cells and their stability issues.
2. Chapter 3 covers a detailed overview of experimental and characterization techniques being used extensively for perovskite film and perovskite solar cells.
3. Chapter 4 describes the experimentation results carried out for perovskite film and perovskite solar cells.
4. Chapter 6 includes the results and discussion.
5. Chapter 6 includes the conclusion and recommendations.

Summary

This chapter describes the need for renewable energy and the importance of solar PV technology among all renewable energy. In this chapter, global and Pakistan solar PV potential has been discussed. Also, the different types of solar energy have been discussed especially the third-generation solar cells. In third-generation solar cells, perovskite solar cells are the most promising ones in achieving high efficiency in a very short period but their stability is the main reason which hinders its commercialization. Moreover, the analysis of different environmental factors affecting the performance of perovskite solar cells has been studied. This chapter also includes the motivation and objectives of this research. The last section is a summary of the outlines of this thesis and how it would proceed.

References

[1] *Global Warming-The Complete Briefing 4th edition*. 2009.

[2] “Statistics CO2 emissions from fuel combustion,” 2016.

[3] U. S. News, W. The report, W. Post, and T. Guardian, *Praise for Plan B*. 2007.

[4] “Renewable capacity highlights Renewable generation capacity by energy source.” Accessed: Jun. 08, 2021. [Online]. Available: www.irena.org/publications.

[5] “BP Statistical Review of World Energy Statistical Review of World,” 2019.

[6] International Renewable Energy Agency and Irena, *RENEWABLE POWER GENERATION COSTS IN 2018*. 2018.

[7] U. S. Energy, “International Energy Outlook 2017 Overview,” 2017.

[8] S. Adnan, N. Drought, M. Centre, A. H. Khan, S. Haider, and R. Mahmood, “Solar energy potential in Pakistan Solar energy potential in Pakistan,” Renewable and Sustainable Energy, Vol. 4, 2012, DOI: 10.1063/1.4712051.

[9] O. Yehezkeli *et al.*, “Integrated photosystem II-based photo-bioelectrochemical cells,” *Nat. Commun.*, vol. 3, no. 1, pp. 1–7, Mar. 2012, DOI: 10.1038/ncomms1741.

[10] “10.7: Diodes, LEDs and Solar Cells - Chemistry LibreTexts.”.

[11] A. Khatibi, F. Razi Astaraei, and M. H. Ahmadi, “Generation and combination of the solar cells: A current model review,” *Energy Science and Engineering*, vol. 7, no. 2. John Wiley and Sons Ltd, pp. 305–322, Apr. 2019, DOI: 10.1002/ese3.292.

Chapter 2

Literature Review

2.1 Background on Perovskite Solar

It is demonstrated that the most adaptable ceramic host is the perovskite structure. Lev Perovski, a well-known geologist at the time, inspired the name of the mineral perovskite, which was initially found in 1839 by Gustav Rose in the Russian Ural Mountains. The newly found mineral's chemical composition was $CaTiO_3$. The oxygen and calcium atoms are arranged in cubic close-packed layers all along the cubic direction in the ideal perovskite, which may also be thought of as a cubic close-packed structure. Ti atoms are present in a few of the resultant octahedral holes. Recent years have seen a lot of interest in a structurally related family of materials called organic-inorganic hybrid perovskites[1]. The perovskite structure is essentially retained in this relatively new family, but at least one ion typically A or X is replaced with an organic ion, turning the perovskite into a hybrid.

Within a specific tolerance, the usual chemical formula for perovskite structure is ABX_3, which results in the perfect perovskite structure. Victor Moritz Goldschmidt first described this tolerance in 1926, and it is known as the Goldschmidt tolerance factor[2].

In the perfect cubic unit cell, the ionic radii determine the cell axis, a. (rA, rB, and rX).

$$a = \sqrt{}\, 2(rA + rX) = 2(rB + rX) \qquad \text{Eq. 1. 1}$$

The Goldschmidt tolerance factor t, which is the ratio between the two cell length expressions, allows us to gauge the degree of distortion as indicated by the equation.

$$t= (rA + rX)\ \sqrt{2}(rB + rX) \qquad \text{Eq. 1. 2}$$

where rA is the radius of the A-cation, rB is the radius of the B-cation, and r is the radius of the anion. The cubic perovskite has t = 1.00. If the size of the A cation decreases then t becomes smaller than 1. However, the cubic structure occurs if $0.89 < t < 1$[3]. The symmetry of the crystalline structure will decrease when t values are reduced. The following illustration depicts the perovskite's ideal cubic structure is shown below in figure 2.1.

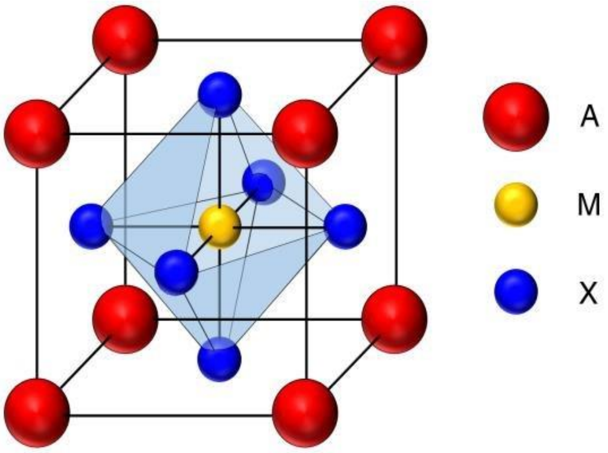

Figure 2.1: Ideal Cubic Structure

The structure of perovskites was the subject of decades of research, and in 2009 the first perovskite solar cell based on the ABX_3 structure was created. This organic-inorganic hybrid perovskite solar cell has an efficiency of 3.8 percent[4] while the highest efficiency thus far is 25.5 percent, as shown in graph 1[5].

2.2 Working on perovskite Solar Cells

Perovskite solar cells are built in a sandwich design, harvesting light through multiple layers of thin sheets [8]. In perovskite solar cells, there are five layers: the FTO substrate, which serves as the electrode; the electron transport layer; the perovskite absorber layer; the hole transport layer; and the top electrode, which is made of Au/Ag. The photoelectric effect and exciton formation serve as the foundation for these cells' operation. Light causes excitons to form in the perovskite; once formed, the holes and electrons move across the layers in the direction of least resistance. The cathode and anode then gather electrons and holes, respectively, to produce a potential difference.

This voltage difference could be used to power a load when it is applied.

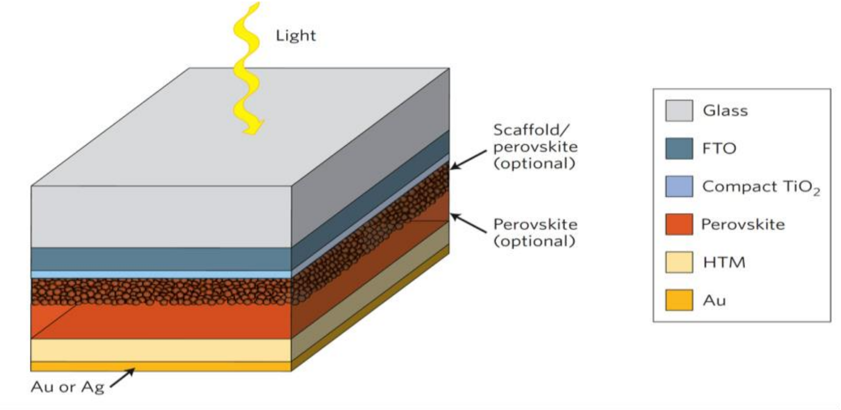

Figure 2.2: Top Electrode Au/Ag[8]

2.3 Band Alignment of Perovskite Solar

The energy level diagram of a perovskite solar cell is shown in Figure 7, which demonstrates how the photoelectric effect can be used to produce power. A perovskite solar cell can allow electrons and holes to be extracted on opposing sides of the cell, producing a potential difference, by leveraging the energy level of various materials. In a cell, holes and electrons will travel in the direction of least resistance. The HOMO and LUMO levels are shown in this diagram. The produced electrons travel from the ETL's LUMO to the LUMO of the perovskite absorber layer. Holes migrate from the HOMO of the HTM to the HOMO of the perovskite absorber layer. Now, holes are captured by the top contact like Ag from the HOMO of the HTM, and electrons are gathered by the FTO from the LUMO of the ETL. To ensure that the gadget performs, the energy level variances should be kept to a minimum [6]figure 2.3.

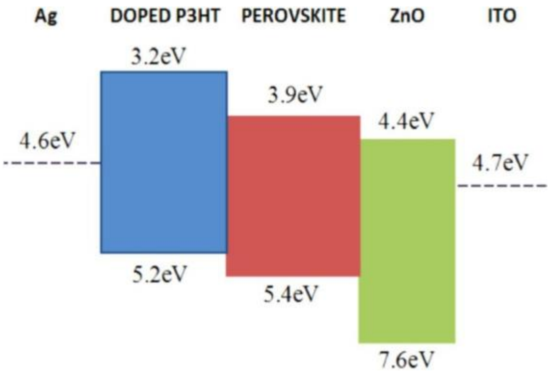

Figure 2.3: Energy Levels Difference **[**6]

2.4 The architecture of perovskite solar cell:

Perovskite solar cells' architecture, which in turn determines the material selection, the deposition techniques for the material, and naturally, the compatibility of the many components in the device, is a major determinant of the device's performance. So far, mesoscopic and planar structures have been established as the two main types of perovskite solar cells. The perovskite can be included in the mesoscopic architecture either as a thin coating that barely covers the oxide scaffold or with charge-transporting material infiltrating the scaffold's pores. However, the high-temperature sintering of the TiO_2 layer required for these mesoporous devices could lengthen processing times and raise the cost of cell production[7].

Long charge carrier diffusion lengths (100 nm for $CH_3NH_3PbI_3$ and 1000 nm for $CH_3NH_3PbI_{3-x}Cl_x$) are characteristic of methylammonium-based perovskites[8][9]. Recently, it was discovered that $CH_3NH_3PbI_3$ single crystals can reach diffusion lengths of more than 175 um[10]. More research revealed the ambipolar behavior of perovskites, proving that these materials are capable of transporting both electrons and holes between the cell terminals[9]. These outcomes all suggested that a planar structure was doable. Through interface engineering, the efficiency of the planar structure was recently increased by about 19 percent[11]. These findings demonstrated that the planar structure might perform devices similarly to the mesoporous structure. According to the type of selective contact utilized on the bottom, the planar structure can be split into two categories: regular (n-i-p) and inverted (p-i-n). Figure 2.5 illustrates both device topologies. An organometal halide perovskite film's morphology, which fundamentally consists of two primary precursor components, is dependent on the method of deposition (solution-based or vacuum-based). Precursors may be placed simultaneously or separately. These permutations together result in a variety of thin-film deposition methods for hybrid perovskite materials. In general, a single deposition results in a more uncontrollable crystallization that results in a diversity of morphologies and, consequently, a spectrum of device performances, without any extra confinement, modification to the composition, or alteration to the crystallization process.

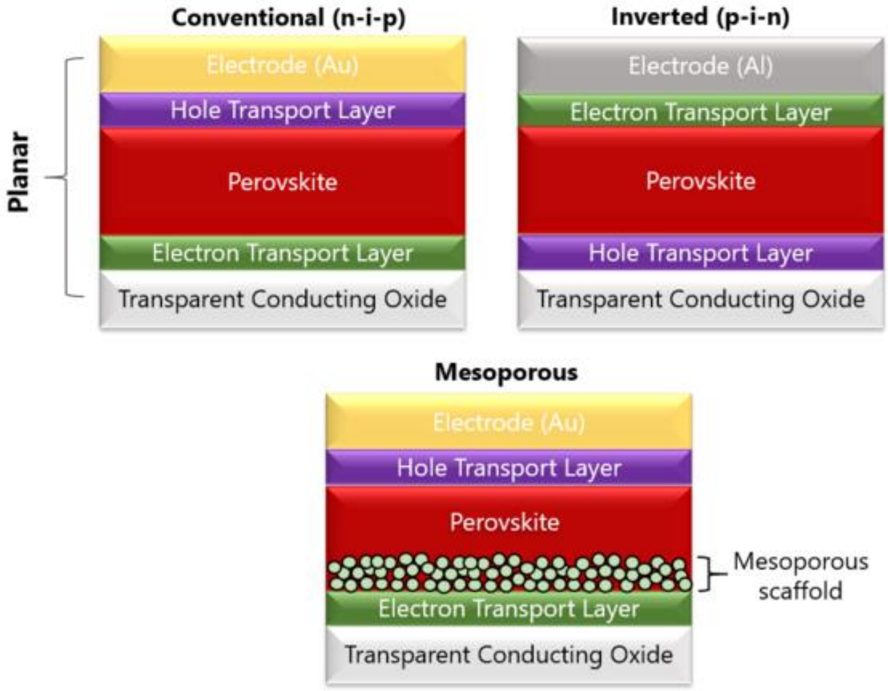

Figure 2.4: Perovskites Planar Structures[11]

2.5 Problems associated with the commercialization

The efficiency of perovskite solar cells is unquestionably high, and they present "a distinct form of the solar cell" that may be inexpensive to produce as well as semi-transparent, light, and flexible.

This type of solar cell's long-term stability, however, is by no means useful. Ex-situ experiments on the long-term durability of $CH_3NH_3PbI_3$ solid-state solar cells kept at room temperature in the absence of encapsulation lasted more than 500 hours under a single sun's illumination and 1000 hours under full sunshine. As a result, it was discovered that light absorption alone is not the main cause of this unstable behavior.

Understanding the precise reasons for the instability of perovskite solar cells is the first step toward enhancing that stability. Numerous causes, which can be generally divided into extrinsic and intrinsic ones, can lead to the breakdown of the perovskite crystal. Below is a discussion of both. both the internal intrinsic factors, such as ion migration, electro-migrations, and interfacial interactions, as well as the exterior factors, such as moisture, oxygen, temperature, UV light, etc.

2.6 Extrinsic Factors

2.6.1 Moisture

Perovskite films can quickly deteriorate in the presence of ambient humidity, particularly in $MAPbI_3$. When excessive humidity is paired with UV light, high temperatures, or the introduction of an electric field, the pace of deterioration will accelerate[12]. Organic cations are particularly hygroscopic and are employed in perovskite solar cells. According to some theories, the water molecules' weak hydrogen interactions with the cations undermine the crystal's structural stability[13][14][15] and As a result, a hydrated perovskite phase may develop. This transformation is undoable.

However, it has been suggested that with enough moisture penetration, the perovskite crystal decomposes. Shown below is a chain of reactions that could be responsible for non-reversible degradation in $MAPbI_3$ perovskites [13].

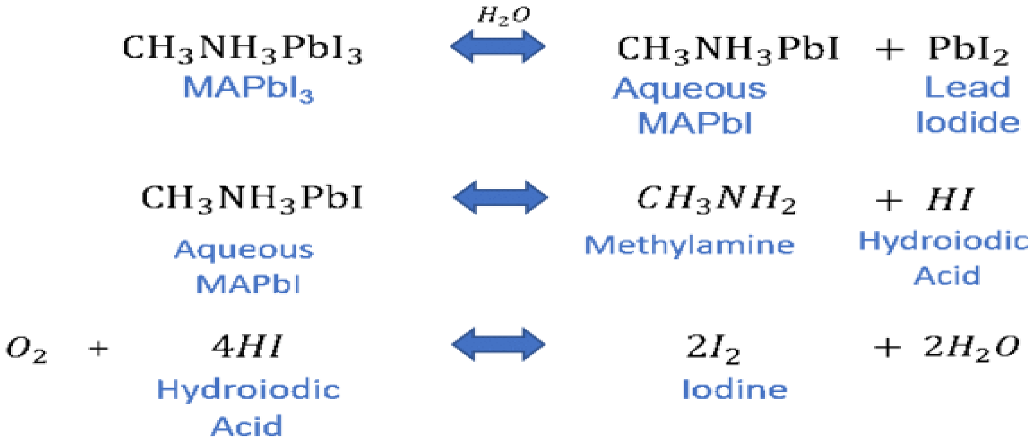

Figure 2.5: Chain of reactions from $MAPbI_3$ perovskites, catalyzed by water [13]

This demonstrates the transformation of $MAPbI_3$ into lead iodide and methylammonium lead iodide (MAI) in an aqueous form (PbI_2). Figure 2.5 illustrates the production of methylamine and hydroiodic acid (HI) from this. More water is then created when oxygen is present. This starts a vicious cycle that further degrades moisture. The development of the perovskite active layer can potentially be affected by the presence of too much PbI_2. Strengthening the bonds between the organic component and the metal halides is one strategy to lessen this effect. Active layers must be laid down in a controlled-humidity setting. It is also possible to add hydrophobic interlayers to assist shield the perovskite from environmental moisture[12].

2.6.2 UV

When other considerations are taken into consideration, UV light's impact on the stability of perovskite solar cells is most significant (e.g. moisture or oxygen exposure). However, it has been demonstrated that $MAPbI_3$ will decay to PbI_2 in the absence of moisture or oxygen when exposed to UV light[16]. Better photostability than $MAPbI_3$ counterparts is one of the key benefits of formamidinium lead iodide ($FAPbI_3$) solar cells[17]. Additionally, the perovskite solar cell's longevity is decreased by the fact that TiO_2, a typical electron-transport layer, is highly vulnerable to UV-induced deterioration[13].

2.6.3 Temperature

Elevated temperature exposure can lead to deterioration. Both $MAPbI_3$ and $MAPbCl_xI_{(3-x)}$ exhibit this[18]. It is believed that at high temperatures, the reactions depicted in Figure 2 can cause $MAPbI_3$ to transform into PbI_2 a result. Though much more slowly than when oxygen and water are present, this is nonetheless possible without them[18][19].

2.6.4 Oxygen-rich/Ambient conditions

The $MAPbI_3$ perovskite films quickly deteriorate in the presence of any UV radiation, high temperature, high humidity, and oxygen combination. Large PbI_2 structures can then be observed in the perovskite film under oxygen-rich circumstances, although this is not the case for layers generated in a nitrogen-rich environment[19]. However, the most uneven layers are those created under ambient conditions, as shown in figure 2.6:

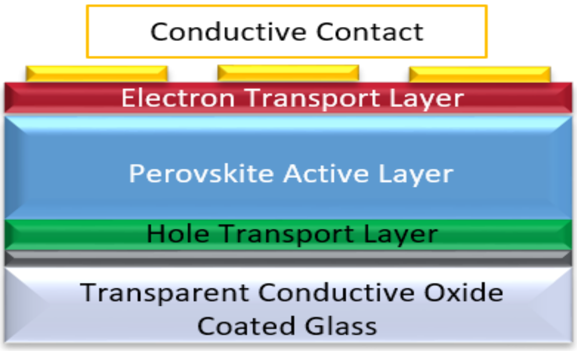

Figure 2.6: Standard layered structure of a perovskite solar cell[19]

The perovskite's surrounding layers may occasionally be a factor in the structural collapse of the material. For instance, the electron-transport layer (ETL) TiO_2 can create trap states when exposed to UV light[20]. A solar cell's efficiency will be severely reduced as a result. This phenomenon can be countered by using an Al-doped TiO_2 or SnO_2[15]

The hole-transport layer is a further layer that significantly affects the performance of a solar cell (HTL). Inorganic HTLs (like P_3HT) and organic HTLs are both possible in perovskite solar cells (e.g. Spiro-OMeTAD). Between the two, there is a trade-off, though. Although Spiro-OMeTAD is a useful HTL, it lacks two additions that would give it appropriate HTL characteristics. The doped Spiro-OMeTAD layer has been criticized for failing to provide the required barrier to shield the perovskite from the elements (air, moisture, etc.)[15]. The organic P_3HT is an alternative that produces a more reliable solar cell. Unfortunately, the efficiency of these cells is lower, as shown in figure 2.6.

2.6.5 Intrinsic Factors

It is typical for the perovskite structure to have vacancies during the production of perovskite films. These flaws could promote ion migration across the perovskite film and are faults (as shown in figure 2.7).

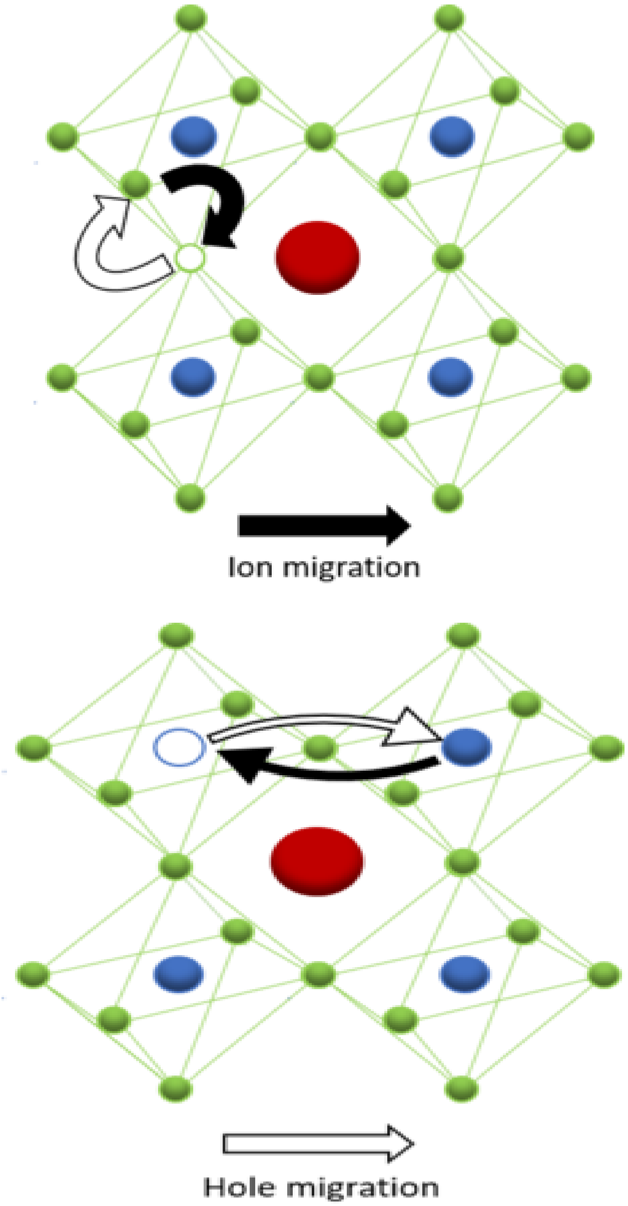

Figure 2.7: Illustrations showing ion and hole migration due to iodide vacancies (left) and metal vacancies (right) through the 3D perovskite structure [21]

Ion migration inside the perovskite layer might cause a PV device's performance to be subpar or inconsistent. For instance, the conductivity of the hole-transport layer Spiro-OMeTAD might be decreased in the presence of migrating iodine ions. The perovskite solar cell's performance is quickly hampered by this[12]. It has been proposed that this ion migration may cause the emergence of a small electric field at the interface of the perovskite material. This might cause the organic cations to deprotonate, which would eventually cause the perovskite solar cell to degrade[12][21].

Perovskite material migration is not the only issue that arises. The perovskite layer can allow ion migration from conductive connections. As a result, the solar cell is short-circuited by creating shunt paths for electrons.

2.7 Effect of the counter electrodes on the perovskite solar cells

PSCs typically have a multilayered device architecture with the absorber "sandwiched" between an electron transport layer (ETL) and a hole transport layer (HTL), with a metal back electrode most frequently Au or Ag completing the circuit. PSCs begin to erode the metal electrode over time as a result of iodine and metal migration, metal halide ion production, the generation of oxygen vacancies, and other factors. This exposes the structure to the environment and results in a steady degradation.[22][23]. A carbon (C) electrode is used in place of a metal electrode in carbon-based perovskite solar cells (C-PSCs). With a suitable work function (WF) of around 5 eV, carbon can serve as an effective charge collector while also acting as a protective barrier for the perovskite layer thanks to its hydrophobic properties, which keep oxygen and moisture out of the environment. In addition, C's inertness makes it immune to the effects of ion migration. This has made it possible to create devices with long-term stability without the use of encapsulation[24]. There are two types C-PSCs:

1. High-temperature carbon electrodes
2. Low temperature carbon electrodes[25].

Both of the structures have the same working principle but there is only one change in the structure of both devices.

2.7.1 High-temperature carbon electrodes

Mesoporous TiO_2 is frequently employed as an electron transport layer in high-temperature C-PSCs. To stop the carbon electrode from coming into touch with the electron transport layer, another mesoporous ZrO_2 or AlO_3 is utilized. The solvents and binders are then evaporated by depositing and annealing a mesoporous carbon electrode at a high temperature. The perovskite absorber material is then applied to the multiple oxide layers, and the triple-stacked layers are penetrated with perovskite before being annealed. With a pure $MAPbI_3$ structure without HTL, the highest efficiency with HT C-PSCs is 16.37 percent

[26]. However, multi-cation technology has recently been found to be the most effective, with a 17.02 percent NiO HTL[27], shown in figure 2.8.

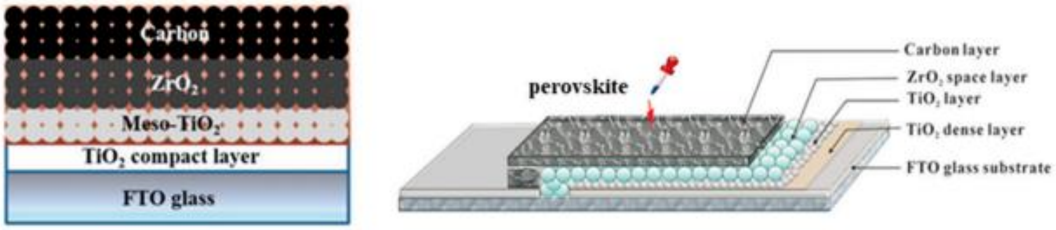

Figure 2.8: A schematic structure of an HTL carbon-based “monolithic” perovskite solar cell[28]

2.7.2 Low-temperature carbon electrodes

Low temperature (LT) C-PSCs, in contrast, have a much more straightforward structure than high temperature (HT) C-PSCs. Perovskite structure, which properly crystallizes at low temperature, was directly deposited carbon electrodes in this structure. Additionally, mesoporous layers are not required; instead, compact layers can be used, improving the device's overall performance and stability. This structure can be used to produce PCE that is comparable to Au- and Ag-based devices. To attain good efficacy and stability, these LC C-PSCs may employ multi-cation and multi-halide architectures, as shown in figure 2.9 [28][29].

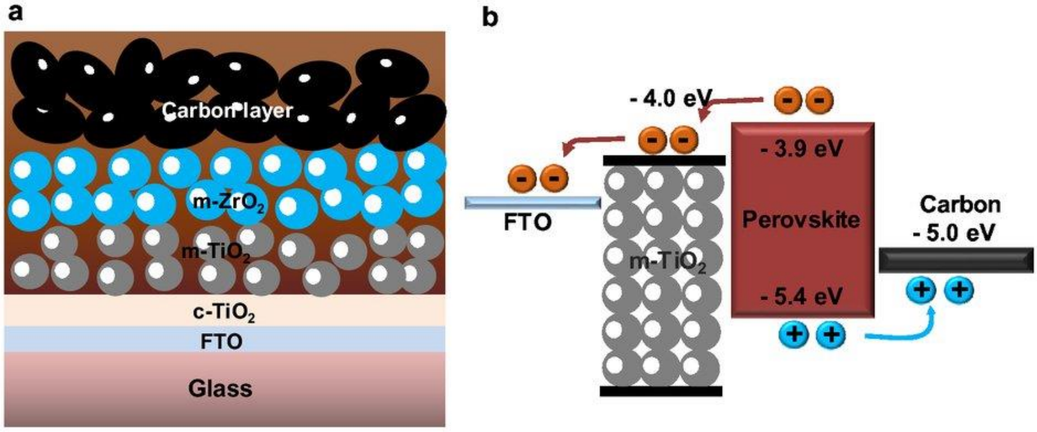

Figure 2.9: Fabrication process of LT "paintable" perovskite solar cells [28]

2.8 Fabrication of the Carbon electrode

High-performing C pastes have been made using a range of carbon materials, producing C electrodes with excellent mechanical stability, low series resistance, and high conductivity. Among these, the mixture of carbon black (CB) and graphite has been proven to be highly effective. Most commonly, carbon black, graphite, polymer, additive, and non-polar solvent are found in carbon pastes. To prevent the disintegration of the underlying perovskite layer in this form of C-PSC, the paste's ingredients must be compatible[30][31], while taking this into account Chlorobenzene was then used to create the paste from the dried carbon by Zhou H. et al. after completely removing the solvent from the commercial carbon paste by drying[32]. Vijayaraghavan et al. created hole transport layer-free C-PSCs using a glass/In doped SnO_2/QD-SnO_2/Perovskite/Carbon device structure. They employed the mixed cation structure $Cs_{0.05}FA_{0.81}MA_{0.14}PbI_{2.55}Br_{0.45}$ and attained 13.64 percent efficiency[33], shown in figure 2.10.

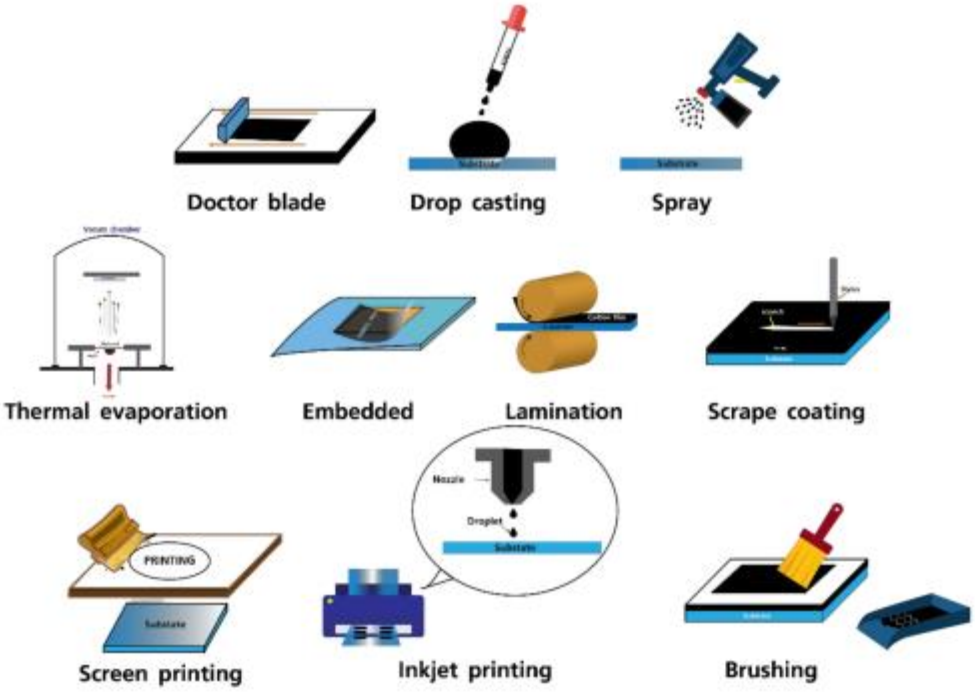

Figure 2.10: Schematic illustration of several techniques for fabrications of carbon electrodes in perovskite solar cells [34]

2.9 Research Idea

Conventional fossil fuels are depleting and also, and they harm the environment. Therefore, the transition from non-renewable to renewable energy technologies is the need of the modern era. Scientists are working to explore new ways to improve the efficiency of these renewable energy resources especially solar cells who have been deployed all over the world. Perovskite solar cells' weak stability, which limits their commercial applicability, is still a significant problem. However, the limited use of perovskite solar cells is due to the expensive cost of noble metallic electrodes and hole-transporting materials (HTMs) (PSCs). For HTMs and noble-metal-free PSCs, carbon materials such as graphene, carbon nanotubes, and carbon paste have been used. This proposed study aims to develop novel perovskite absorber materials and charge carrier transfer layers in the ambient conditions to enhance the stability of existing PSCs by controlling the morphology, grain size boundaries, grain size, charge recombination, trap defect states, and hysteresis. The efficiency and stability of perovskite solar cells will be improved through the use of CsBr doping with carbon as a counter electrode, and production costs will be significantly reduced, making perovskite solar cells a commercially feasible next-generation thin-film PV technology.

Summary

Although perovskite solar cells have very high efficiency and are a great alternative to first-generation solar cells, their stability is their only drawback. Perovskites are discovered to be hygroscopic in nature, oxygen, UV light, light soaking, heat, and other possible variables, as was previously stated. The perovskite may become damaged as a result of the development of hydrate intermediates brought on by moisture and oxygen. Initially, the majority of PSCs were formed from MA, and it has been demonstrated that due to the volatility of the organic MA, $(MA)PbX_3$ compounds decompose at 85 °C. Due to its high hygroscopicity, FA is also more sensitive to moisture than MA, which raises the cost and necessitates more stringent encapsulation. The thermal stability of Cs-based perovskite should be greater than that of FA- and MA-based equivalents. However, compared to MAPbI3 and $(MAPbBr_3)_x(FAPbI_3)_{1x}$, the PCE for Cs-based perovskites is considerably lower due to the non-ideal band gaps (>1.7 eV). So, to create perovskite, researchers began using a mixture of Cs/MA or Cs/MA/FA, etc. It was discovered that the use of Cs improved device performance by stabilizing the black phase of FAPbI3 and reducing trap states. To boost stability in our project, we will add a small amount of Cs/FA in MA at the A-site cation. Additionally, by partially substituting the relatively smaller Br ion for the large I anion, we should be able to stabilize the structure and create $CsPb(Br_xI_{1-x})_3$ perovskites that are thermodynamically advantageous at normal temperature. While $CsPbI_3$ in the cubic perovskite phase has a more desirable band gap of 1.73 eV and is stable in air at room temperature, it transitions to a yellow, insulating, non-perovskite phase known as the -phase at temperatures below 315 C. This is because $CsPbBr_3$ has an orthorhombic perovskite with a band gap of 2.25 eV and is stable in air. Therefore, by adjusting the halide concentration and stabilizing our cell, it is possible to regulate the bandgap of (CH_3NH_3) Pb $(Br_xI_{1-x})_3$ between 2.3 and 1.9 eV. However, the carbon CE, which tends to be hydrophobic, will take the place of the currently utilized hole transport layer, potentially improving the stability of PSCs as a whole.

References

[1] E. Article, G. Kieslich, S. Sun, and A. K. Cheetham, "An extended Tolerance Factor approach for organic-inorganic perovskites †," Chemical Science, pp. 3430–3433, 2015, DOI: 10.1039/c5sc00961h.

[2] T. Sato, S. Takagi, S. Deledda, B. C. Hardback, and S. Orimo, "Extending the applicability of the Goldschmidt tolerance factor to arbitrary ionic compounds," *Nat. Publ. Gr.*, no. March, pp. 1–10, 2016, DOI: 10.1038/srep23592.

[3] M. Johnsson and P. Lemmens, "Perovskites and thin films — crystallography and chemistry," Phys. Condens Matter, pp. 20-26, 2008, DOI: 10.1088/0953-8984/20/26/264001.

[4] A. Kojima, K. Teshima, Y. Shirai, and T. Miyasaka, "Organometal Halide Perovskites as Visible-Light Sensitizers for Photovoltaic," J. Am. Chem. Soc. pp. 6050–6051, 2009.

[5] US National Renewable Energy Laboratory, "Best Research-Cell Efficiencies," *NREL*. p. 1, 2019.

[6] M. Ye, C. He, J. Iocozzia, X. Liu, and X. Cui, "Recent advances in interfacial engineering of perovskite solar cells," Applied Physics, pp.16 DOI:10.1088/1361-6463/aa7cb0 2017.

[7] T. Salim, S. Sun, Y. Abe, A. Krishna, A. C. Grimsdale, and Y. M. Lam, "and device architecture on device performance," *J. Mater. Chem. A Mater. energy Sustain.*, vol. 3, pp. 8943–8969, 2015, DOI: 10.1039/C4TA05226A.

[8] S. D. Stranks *et al.*, "Electron-Hole Diffusion Lengths Exceeding,", Science, vol. 341, no. 2013, 2014, DOI: 10.1126/science.1243982.

[9] O. C. H. N. H. Pbi and G. Xing, "Long-Range Balanced Electron-," Science vol. 344, no. 2013, 2014, DOI: 10.1126/science.1243167.

[10] Q. Dong, Y. Fang, Y. Shao, J. Qiu, L. Cao, and J. Huang, "Electron-hole diffusion lengths > 175 μm in solution-grown CH 3 NH 3 PbI 3 single," Science, pp. 1–8, 2015, DOI:10.1126/science.aaa5760.

[11] W.S. Yang, J.H. Noh, N.J. Jeon, Y . C. Kim, S. Ryu, J. Seo, S. Il Seok, "High-performance photovoltaic perovskite layers fabricated through intramolecular exchange," Science Vol.80, pp. 1234-1237, 2015

DOI:10.1126/SCIENCE.AAA9272.

[12] A. Rajagopal, K. Yao, and A. K. Jen, “Toward Perovskite Solar Cell Commercialization : A Perspective and Research Roadmap Based on Interfacial Engineering,” vol. 1800455, pp. 1–45, 2018, DOI: 10.1002/adma.201800455.

[13] S. Emami, L. Andrade, and A. Mendes, “Recent progress in the long-term stability of perovskite solar cells,” Advance Science, vol. 2, pp. 52–62, 2015, DOI: 10.24840/2183-6493.

[14] G. E. Eperon *et al.*, “The Importance of Moisture in Hybrid Lead Halide Perovskite Thin Film Fabrication,” ACS Nano, pp. 9380–9393, 2015, DOI: 10.1021/acsnano.5b03626.

[15] D. Wang, M. Wright, N. K. Elumalai, and A. Uddin, “Solar Energy Materials & Solar Cells Stability of perovskite solar cells,” *Sol. Energy Mater. Sol. Cells*, vol. 147, pp. 255–275, 2016, DOI: 10.1016/j.solmat.2015.12.025.

[16] S. Lee *et al.*, “OPEN UV Degradation and Recovery of Perovskite Solar Cells,” *Nat. Publ. Gr.*, pp. 1–10, 2016, DOI: 10.1038/srep38150.

[17] J. Lee, D. Kim, H. Kim, S. Seo, S. M. Cho, and N. Park, “Formamidinium and Cesium Hybridization for Photo- and Moisture-Stable Perovskite Solar Cell,” Advanced Energy Materials, Vol. 5, pp. 507-510, 2015, DOI: 10.1002/aenm.201501310.

[18] B. Philippe, B. Park, R. Lindblad, J. Oscarsson, S. Ahmadi, and E. M. J. Johansson, “Chemical and Electronic Structure Characterization of Lead Halide Perovskites and Stability Behavior under Different Exposures A Photoelectron Spectroscopy Investigation,” Chem. Matter, Vol. 5, pp. 1720-1731, 2015, DOI: 10.1021/acs.chemmater.5b00348.

[19] B. Conings *et al.*, “Intrinsic Thermal Instability of Methylammonium Lead Trihalide Perovskite,” Advanced Energy Materials, Vol. 5, pp. 1–8, 2020, DOI: 10.1002/aenm.201500477.

[20] S. K. Pathak *et al.*, “Performance and Stability Enhancement of Dye-Sensitized and Perovskite Solar Cells by Al Doping of TiO 2,” Advanced Functional Materials, Vol.24, pp. 1–10, 2014, DOI: 10.1002/adfm.201401658.

[21] Sajedi Alvar et al., “Absence of ferroelectricity in methylammonium lead iodide perovskite,” Energy & Environmental Science, Vol. 7, 2015, DOI: 10.1039/C5EE01265A.

[22] T. A. Berhe *et al.*, “Organometal halide perovskite solar cells: degradation and stability,” *Energy Environ. Sci.*, vol. 9, no. 2, pp. 323–356, Feb. 2016, DOI: 10.1039/C5EE02733K.

[23] J. Wang *et al.*, “Electrochemical Corrosion of Ag Electrode in the Silver Grid Electrode-Based Flexible Perovskite Solar Cells and the Suppression Method,” *Sol. RRL*, vol. 2, no. 9, p. 1800118, Sep. 2018, DOI: 10.1002/SOLR.201800118.

[24] G. Grancini *et al.*, “One-Year stable perovskite solar cells by 2D/3D interface engineering,” *Nat. Commun. 2017 81*, vol. 8, no. 1, pp. 1–8, Jun. 2017, DOI: 10.1038/ncomms15684.

[25] D. Bogachuk *et al.*, “Low-temperature carbon-based electrodes in perovskite solar cells,” *Energy Environ. Sci.*, vol. 13, no. 11, pp. 3880–3916, Nov. 2020, DOI: 10.1039/D0EE02175J.

[26] M. Que, B. Zhang, J. Chen, X. Yin, and S. Yun, “Carbon-based electrodes for perovskite solar cells,” *Mater. Adv.*, vol. 2, no. 17, pp. 5560–5579, Aug. 2021, DOI: 10.1039/D1MA00352F.

[27] S. Liu *et al.*, “17% efficient printable mesoscopic PIN metal oxide framework perovskite solar cells using cesium-containing triple cation perovskite,” *J. Mater. Chem. A* vol. 5, no. 44, pp. 22952–22958, Nov. 2017, DOI: 10.1039/C7TA07660F.

[28] M. Bidikoudi, C. Simal, and E. Stathatos, “Low-Toxicity Perovskite Applications in Carbon Electrode Perovskite Solar Cells—A Review,” *Electron. 2021, Vol. 10, Page 1145*, vol. 10, no. 10, p. 1145, May 2021, DOI: 10.3390/ELECTRONICS10101145.

[29] H. Zhang *et al.*, “Self-Adhesive Macroporous Carbon Electrodes for Efficient and Stable Perovskite Solar Cells,” *Adv. Funct. Mater.*, vol. 28, no. 39, p. 1802985, Sep. 2018, DOI: 10.1002/ADFM.201802985.

[30] Z. Ku, Y. Rong, M. Xu, T. Liu, and H. Han, “Full Printable Processed

Mesoscopic CH3NH3PbI3/TiO2 Heterojunction Solar Cells with Carbon Counter Electrode,” *Sci. Reports 2013 31*, vol. 3, no. 1, pp. 1–5, Nov. 2013, DOI: 10.1038/srep03132.

[31] A. Mei *et al.*, “A hole-conductor-free, fully printable mesoscopic perovskite solar cell with high stability,” *Science (80-.).*, vol. 345, no. 6194, pp. 295–298, Jul. 2014, DOI: 10.1126/SCIENCE.1254763/SUPPL_FILE/MEI.SM.PDF.

[32] P. Kartikay, A. Yella, and S. Mallick, “Binder-solvent effects on low temperature-processed carbon-based, hole-transport layer free perovskite solar cells,” *Mater. Chem. Phys.*, vol. 256, Dec. 2020, DOI: 10.1016/J.MATCHEMPHYS.2020.123594.

[33] S. N. Vijayaraghavan, J. Wall, L. Li, G. Xing, Q. Zhang, and F. Yan, “Low-temperature processed highly efficient hole transport layer free carbon-based planar perovskite solar cells with SnO2 quantum dot electron transport layer,” *Mater. Today Phys.*, vol. 13, Jun. 2020, DOI: 10.1016/J.MTPHYS.2020.100204.

[34] P. Pradid, K. Sanglee, N. Thongprong, and S. Chuangchote, “Carbon electrodes in perovskite photovoltaics,” *Materials (Basel).*, vol. 14, no. 20, pp. 1–14, 2021, DOI: 10.3390/ma14205989

Chapter 3

Introduction to Fabrication and Characterization Techniques

3.1 Fabrication Techniques

Perovskites absorber layer and perovskite solar cells are fabricated by using the following fabrication techniques:

- Spin Coater
- Glove Box

3.1.1 Spin Coating

Spin coating is a common deposition technique for thin film application. it is employed in a plethora of applications in many industries. The advantages of spin coaling are that it is easy, quick, and capable of producing uniform films of thickness ranging from nanometers to a few microns, as shown in figure 3.1[1].

3.1.1.1 Working Principle

The technique requires the deposition of a thin film on the substrate surface by creating a solution containing the compound dissolved in the solvent and rotating it at low or high speeds.

The step-by-step procedure is given as:

1. The substrate is covered with the solution with the desired material dissolved in a compatible solvent
2. High seed rotation of the substrate allows most of the solvent to fly off to the side.
3. The substrate is dried to evaporate the remaining solvent and obtain a layer of the desired molecules.

At high rotations seeds (up to 12,000 rpm) the centripetal force coupled with the surface tension associated with the solution and substrate interface pulls the coating to all sides resulting in even coverage. The solvent also evaporates during the sinning and the film is further annealed to completely dry it off[1][2].

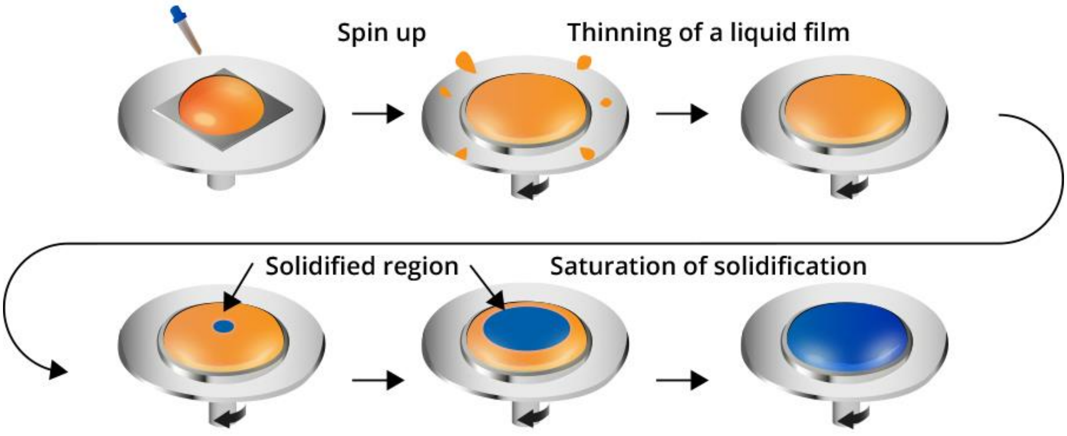

Figure 3.1:Spin coating technique for coating thin films**[1]**

3.1.1.2 Thickness Equation

The thickness of the spin-coated film depends on the spin see and angular velocity. The thickness is inversely proportional to the revolutions per minute at which the substrate is rotated.

$$t \propto \frac{1}{\sqrt{\omega}} \qquad \text{(Eq.3.1)}$$

Where

- t is the layer's thickness
- ω is the angular velocity.

3.1.2 Glove Box

Glove Boxes are used by radiochemical, metallurgical, and fabrication laboratories. It consists of a safety glass screen for visibility and vacuum-sealed gloves for safe handling of materials inside the box, as shown in figure 3.2[3].

Figure 3.2:Glove Box System [3]

A glove box can be compared to a fume hood except that it has an exhaust system, and the inside environment is strictly controlled. The box is completely closed to prevent from entering and there are only arm-length gloves to allow experiments to be performed within the equipment. An inert gas like argon and nitrogen can be used to bring down the oxygen and moisture level to less than 0.1ppm. A purifier or filter is fitted inside the glove box to seal the gas and maintain an inert environment[4].

3.2 Characterization Techniques

For the characterization of the perovskite absorber layer following techniques were used:

- Optical Characterization
- Morphological Characterization
- Structural Characterization

3.2.1 Optical Characterizations

The following equipment was used for the optical characterization:

- UV-Vis Spectroscopy
- Photoluminescence spectroscopy

- Optical profilometry spectroscopy

3.2.1.1 UV-Vis spectroscopy

Using an ultraviolet-visible (UV-Vis) spectrophotometer, the diffuse reflectance of nanostructures placed over a glass substrate was evaluated to determine the optical measures of structures such as absorbance (PerkinElmer, Lambda 950). UV-visible spectroscopy also known as “electronic spectroscopy” is a technique used to determine the bandgap energy of the semiconductor employed for the photo-activity, shown in figure 3.2. The absorption of UV-visible irradiation from a specimen can be determined by ultra violet-visible spectroscopy with single wave lengths or scans over a range within a spectrum. The UV light wavelength lengthens from 200-400 nm while the wavelength of the visible spectrum ranges from 400-800 nm. The concentration of electromagnetic energy from the UV-visible spectrum stimulates an electron fervor from conduction to valance energy states. The light absorbance of any absorbing substance is directed through Lambert-Beer law which defines as while keeping the specimen thickness constant when radiation of a particular wavelength passes through the compartment of the sample, it causes the absorbance of light that gives the results. The Lambert-Beer Law mathematically can be formulated as follows [8];

$$A = \mathcal{E} l c \qquad \textbf{Eq 3. 2}$$

Where A is absorbance or optical density, Ɛ is epsilon (molar absorption coefficient of the analyte having a specific wavelength), where l is the specimen's route length and c is the analyte concentration,

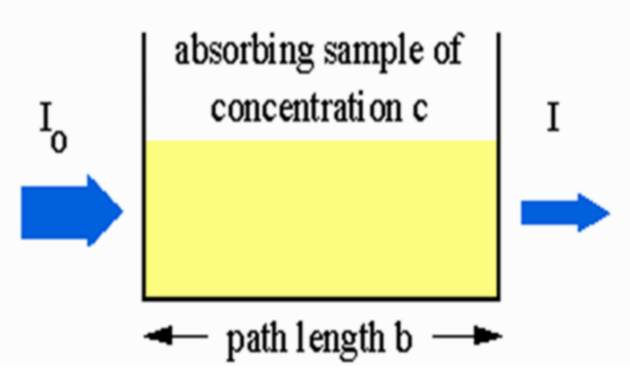

Figure 3.3:The basic principle of Lambert-Beer Law adopted[9]

I0 is the amount of light that is incident, and I am the amount of light that has passed through the sample, shown in figure 3.3.

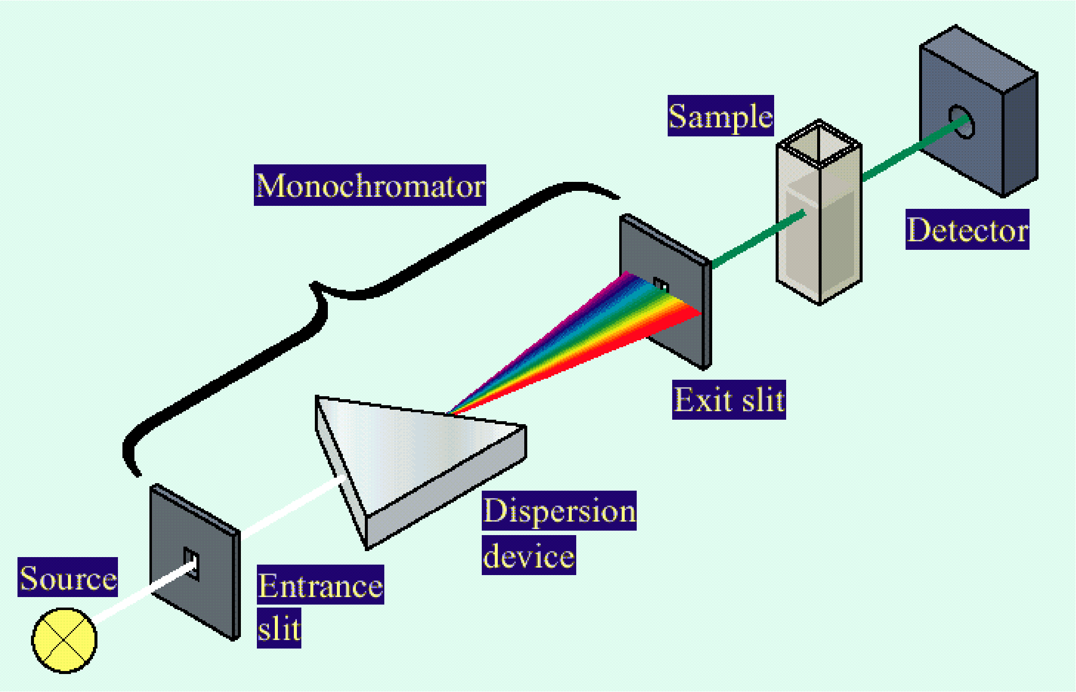

Figure 3.4:The fundamental principle of UV-visible spectroscopy[8]

3.2.1.2 Band gap analysis

The spectrum of UV-Vis is used to calculate the energy bandgap, this determines the relationship between the absorption coefficient by the absorption edge and the optical band gap. Diffuse reflectance spectra are the simple way to measure the band gap in this study, Kubelka-Munk model is the foremost way for band gap analysis [10]. Following equation being followed;

$$(\boldsymbol{\alpha h v})^2 = (\boldsymbol{h v} - \boldsymbol{E_g}) \qquad \text{Eq. 3.3}$$

$\boldsymbol{\alpha}$ = Absorption constant, based on the effective masses related to the VB and CB

hv = Photon Energy

3.2.1.3 Photoluminescence spectroscopy

The process through which light energy, or photons, promotes the emission of a photon from any substance is known as photoluminescence spectroscopy, or PL for short. It is a way of material probing that is non-contact and non-destructive. Essentially, light is shone onto the sample, where it is absorbed and a process known as photo-excitation can take place. As the material relaxes and returns to a lower energy level after photo-excitation, it will release energy (photons). Photo-excitation causes the material to jump to a higher electronic state. Photoluminescence, abbreviated as PL, is the emission of light or luminescence as a result of this process. Band gap, impurity levels, flaws, recombination process, materials selection, structural properties, and crystallinity are all measured using it[16].

3.2.1.3.1 Working Principle

An analytical tool called Spectro fluorometer records and measures the fluorescence from a sample. To capture the fluorescence, the excitation, emission, or both wavelengths are scanned. Through additional attachments, it is possible to monitor the examination of signal deviation concerning time, temperature, concentration, polarisation, or other variables. Figure 3.5 depicts the fluorescence spectrometer block diagram. Monochromators (wavelength selectors), laser sources (sample illumination), detectors, and corrected spectra are all components of fluorescence spectrometers.[17]

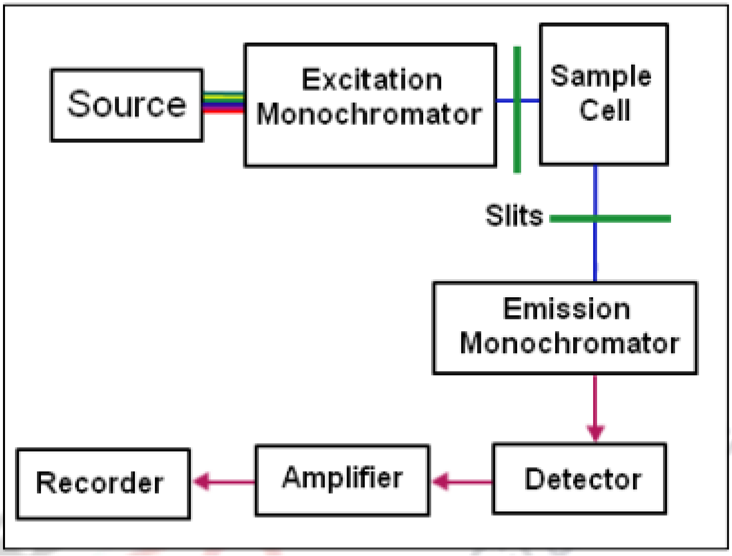

Figure 3.5:Fluorescence spectrometer block diagram[18]

- **Source of Illumination**

A continuous type, 150 W ozone-free xenon arc lamp is the light source employed. A diamond-turned elliptical-shaped mirror collects the light from the lamps, which is then focused into the entry slit of the excitation monochromator. The excitation monochromator is separated from the lamp housing by a quartz-based window, which also serves to vent heat from the device and protect against the improbable event of a lamp failure. Stretching and reducing spherical aberrations and re-diffraction are two benefits of resolution across the entire spectrum.[18]

- **Monochromators**

Excitation and emission monochromators are the two different types of monochromators. It makes advantage of the entire reflective optics to maintain excellent resolution across the entire spectrum and to lessen spherical and re-diffraction aberrations.

- **Gratings**

Reflection To scatter striking (incidental) light through channels that are positioned vertically, the grating is an essential component of a monochromator. Spectra are collected by rotating a grating with 1200 grooves per millimeter that are excited at 330 nm and blazed at 500 nm (emission). The grating is covered in a protective film of MgF_2 to prevent oxidation.

- **Slits**

At the entrance and exit sites of the monochromator, extremely flexible slits are employed. The excitation monochromator's slit width controls the incident light's bandpass, whereas the emission monochromator's slits govern the fluorescence intensity signal, which is controlled (and recorded by the signal detector). The trade-off for determining slit width is between signal strength and spectral resolution. Wider slits result in lower resolution since more light hits both the sample and the detector, whereas using narrower slits results in higher resolution but at the expense of signal.

- **Shutters**

An excitation shutter is positioned beneath the exit slit of the excitation monochromator to protect the sample from photobleaching or photodegradation caused by prolonged exposure to light. Through an emission shutter that is placed directly before the entry of the emission monochromator, the detector is shielded from the strong light.

- **Sample compartment**

There are several possible attachments and bundles of fiber optics in the sample compartment that can be used to transport the excitation beam to a sample that is located far away and the emission beam back to the emission monochromator.

- **Detectors**

There are two different kinds of detectors: reference and signal detectors. An R928P photomultiplier tube that sends the signal to a photon counting module serves as the signal detector, which is based on photon counting. The reference detector's job is to keep an eye on the xenon lamp so that it can be corrected for its time- and wavelength-dependent output. This UV-enhanced silicon photodiode-based detector is situated right before the sample chamber[19].

3.2.1.4 Profilometry

A profiler is an instrument that is to characterize the topography of the uppermost layers of a film and measure its overall thickness. It has multiple points which measure the variation in the texture of a surface at the sub-micron level. The analysis is used to determine the surface roughness and fractality[13].

3.2.1.4.1 Working Principle

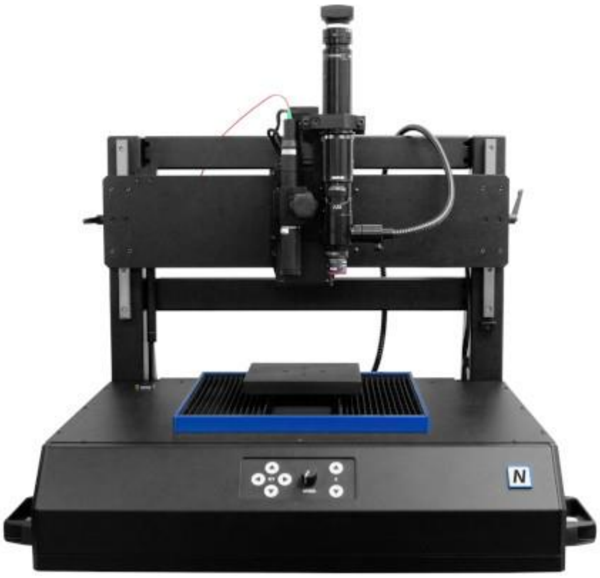

Figure 3.6: Optical Profilometry [13]

Non-contact surface profilometers utilize a range of optical techniques to find out information about a surface’s topography. An incident light source illuminates the surface during scanning. It measures the reflective, refractive, and emissive light to put together information about the surface topography, as shown in figure 3.6. This method is preferred over the contact profilers because it is not invasive and offers faster measurement[14][15].

3.2.2 Structural Characterizations

The following equipment was used for the Structural characterization:

- **X-Ray Diffractometer**

3.2.2.1 X-Ray powder diffraction

X-Ray Diffraction analysis instrument has a very significant and valuable apparatus which characterized the various specimens, to observe lattice parameters as well as for analysis of crystalline phase and their alignment. Catalysts have undergone in-depth research and characterization. The powder was subjected to X-ray diffractometry (XRD) using XRD equipment (Bruker, D8 advanced) equipped with a 25-kV power supply and a Cu K radiation (= 1.5418) source. The data were gathered using a 0.02° step scan and a range of 20 to 70 degrees. The least harmful method for examining a material's structural properties is X-ray diffraction (XRD). By using X-rays on a material, XRD has investigated the internal structure qualities of the substance. Different morphological and structural details of produced nanomaterials are ascertained using the X-ray diffraction (XRD) technique.

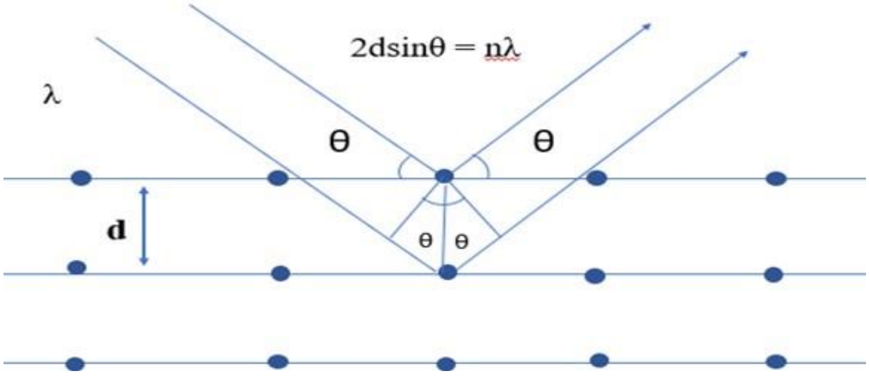

Figure 3.7:X-ray diffraction of crystal lattice planes having layers of the material adopted from reference[5]

This technique is well known for the determination of phase purity and dimensions of crystalline materials in the field of material science. This technique is provided information about atoms' positions and symmetry shape, size, and atomic spacing of atoms in the unit cell of solid materials. Crystalline material and the interference x-rays are the results of specimens given by this technique [5]. In the x-ray diffraction technique, through a cathode ray tube generation of x-rays occurs and after the process of filtration, monochromatic light is emitted. This monochromatic light is concentrated on to sample material. When incident rays interact with to sample it makes constructive interference and follows Bragg’s law, shown in figure 3.7 [6]:

$$\mathbf{2d\sin\theta = n\lambda} \qquad \text{Eq. 3.4}$$

An integer is identified by alphabet n, while λ represents X-ray wavelength, the interplanar spacing of catalyst that results in diffraction is d and u is the angle of diffraction. Bragg’s law helps to recount the electromagnetic radiation wavelength according to diffraction angle and spacing lattice crystalline sample. During X-ray powder diffraction, the scanning made incident angle that varied from 10° to 80° at a scanning rate of 10° per min using Cu Kα radiations λ =1.5405 Å. After diffraction x-rays are then easily identified and calculated. A filament is heated by applying a voltage to the cathode ray tube that emits x-rays to generate electrons. These accelerated electrons are bombarded on the surface of a sample. When these accelerated electrons have gained adequate energy remove the inner shell electrons to move them to a higher energy level after that these electrons lose their energy, and move to a low energy level by emitting a photon. The emitted photons with a specific wavelength show the characteristic of the sample material. Through analysis of x-ray emission spectrum which gives qualitative results about the structure of sample material. These spectra contain different components, the most common being K_α and K_β [6].

3.2.3 Morphological Characterizations

The following equipment was used for the morphological characterization:

- Scanning Electron Microscopy
- Atomic Force Microscopy
- Contact Angle

3.2.3.1 Scanning electron microscopy (SEM)

SEM is an electron microscope type which capable of developing high-resolution images of a sample. Its image has a three-dimensional appearance and is useful for surface structure observation samples. The different morphologies of Zinc oxide Nanostructure were observed by using SEM. The electrons produced by the hot filament are acquired by electric and magnetic fields. These excited electrons interact with sample material to initiate the signals and these signals are containing the information on the surface morphologies of materials. Scanning electron microscopy is an analytical technique that is used to examine the external morphologies, shapes, chemical composition, size, and arrangements of atoms that make up the samples. In this technique, when a sample is hit with a beam of high-energy electrons, which is known as an incident beam that strikes the surface of a solid sample to generate secondary electrons (signals). These secondary electrons are counted by a positively charged electron detector which reveals a two or three-dimension image of the sample including information regarding the variety of shapes, size, composition, and topography of the sample [7]. The size and the shape of nanostructures were studied by using scanning electron microscopy (TESCAN-VEGA-3). The schematic of its working is shown below in figure 3.8.

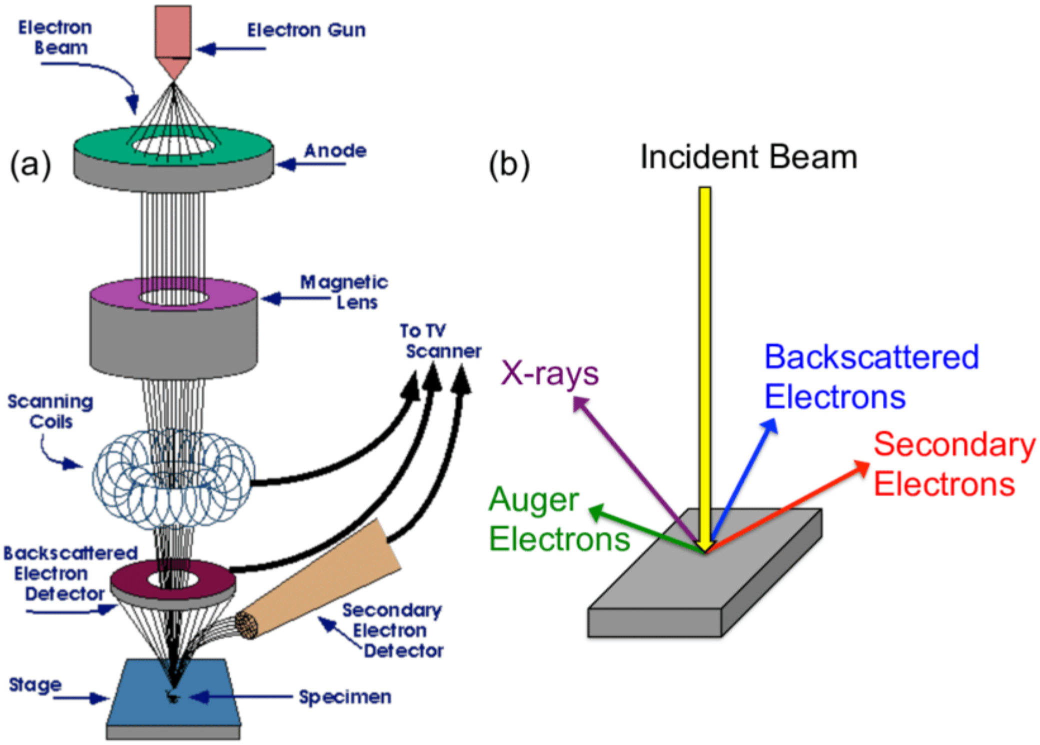

Figure 3.8:Schematic drawing of Scanning Electron Microscope (SEM)[7]

SEM images were examined with a magnification of 5µm-500nm with an accelerating voltage of 15.0-10.0kV. Energy-dispersive X-ray spectroscopy (EDS) allows the target surface analysis and is widely used for material surface analysis. This provides elemental identification and quantitative compositional information. EDS analyses are performed on the same apparatus as for SEM (TESCAN-VEGA-3) by adjusting the voltage at 20kV and width to 15mm. IR camera view was turned off to acquire the spectrum for the site of interest.

3.2.3.2 **Atomic *Force Microscopy***

Atomic force microscopy or AFM is a surface analysis technique that is useful for studying the coatings at a micro or Nanoscale, as shown in figure 3.9. Microscopy can be used to obtain images at a nanoscale range to study the air or liquid sample. The

AFM can be used for high-resolution imaging of many different surfaces to determine surface morphology, roughness, and texture. The tip senses the chemical atoms by forming chemical bonds with them. The interaction after the vibrational frequency and these changes are mapped out by the program[11].

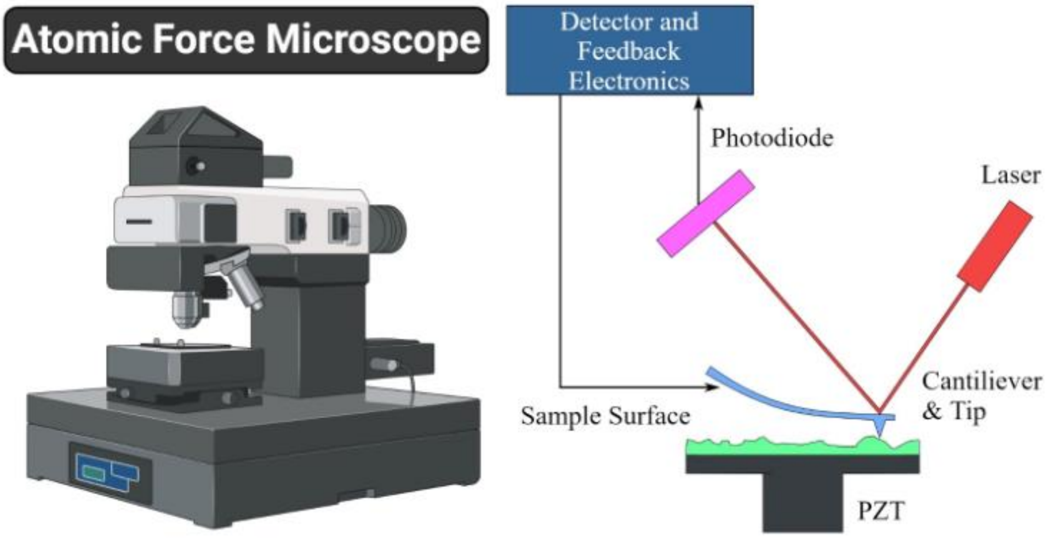

Figure 3 9: Atomic Force Microscopy[11]

3.2.3.3 Working Principle

AFM uses a sharp tip with a diameter of around 10 to 20nm to measure the surface's properties. A cantilever is attached to the tip which is made of silicon or silicon nitride. The movement of the tip is recorded by a laser beam emitted by a photodiode[12].

The equipment operates in two different modes, i.e., the tapping and contact mode. The AFM tip and the surface are in constant contact during the contact mode. This measurement mode is only for specific applications such as that of the force curve. For tapping mode, the cantilever moves to allow only brief contact of the tip with the sample. It is the recommended mode of operation for standard AFM[11].

3.2.3.4 Contact Angle

When a liquid drop is deposited on a material substrate and takes the shape of a dome, a contact angle (also known as a wetting angle) is created. The contact angle, depicted in figure 3.10, is the angle produced between the surface and the line perpendicular to the edge of the water drop, shown in figure 3.10.

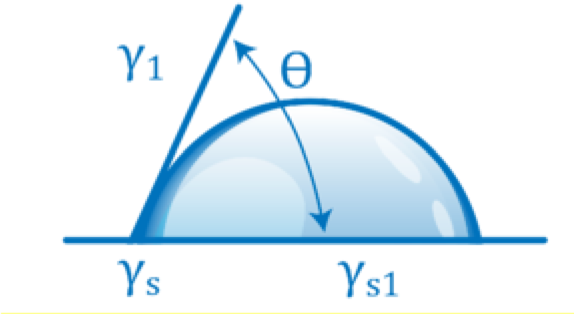

Figure 3.10: Contact Angle Measurement[20]

Figure 3.11: Contact Angle Apparatus[20]

The degree of contact between a liquid and its limiting surface is determined by wettability. Hydrophilicity and hydrophobicity are two more names used to define wettability. Material that exhibits an affinity for water is said to be hydrophilic, whereas the reverse is said to be hydrophobic. Hydrogen bonds can be created between hydrophilic substances and water. The contact angle between a liquid and a solid substrate when the liquid is either stationary or slowly flowing over the surface can be used to determine how hydrophilic a surface is. Figure 3.11 demonstrates how the degree of hydrophilicity affects the contact angle and droplet shape[20].

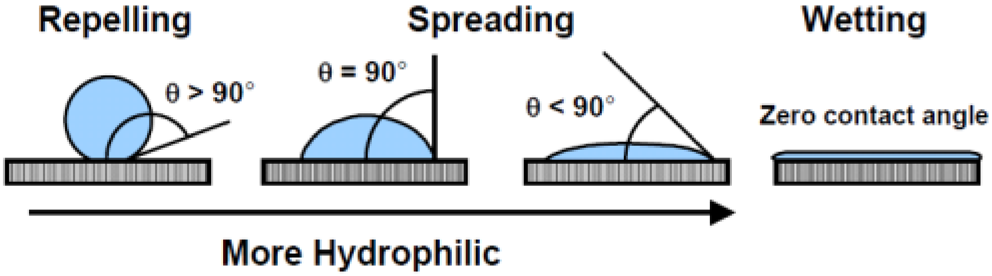

Figure 3.12: Contact angles and hydrophilicity[20]

3.2.3.5 Working Principle

- The micropipette is put within a plastic holder and filled with deionized water.
- As the level brings the surface layer into contact with the liquid, the droplet is manually dispensed at the tip.
- The VCA software program, as depicted in Figure 3, produces the droplet on the sample's surface and then records the image on a CCD camera.
- The software will be used to measure the angles.
- The procedure must be carried out again for various areas of the sample.

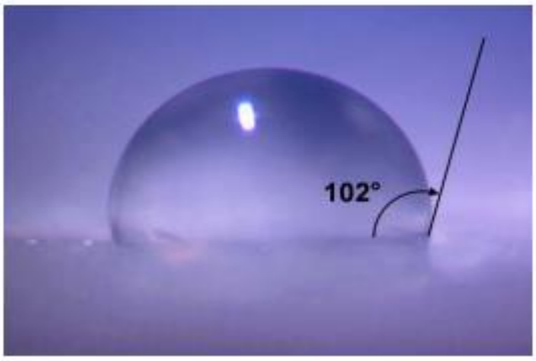

Figure 3.13: Contact angle of water droplet measured on a silicon substrate[20]

3.2.4 Photovoltaic Characterization

For photovoltaic characterization following techniques were used:

- Solar IV Simulator
- External Quantum Efficiency

For IV measurements, the Newport Oriel IV unit with a Keithley PVIV 2400 source meter and solar simulator under a 750 W/m2 power intensity was employed. To block out excess light, the cell was covered with a black mask with an active area of 0.00625 cm^2 [16]. A reference Si photodiode that had been calibrated by Newport at (100 W m^{-2}) was used to calibrate simulator's output light intensity at (1000 Wm^{-2}). Important metrics including open circuit voltage (V_{oc}), short circuit current density (J_{sc}), fill factor (FF), and photoconversion efficiency can be calculated using the J-V data the sampled materials. In figure 3.14 below, a typical J-V curve for solar cells is depicted.

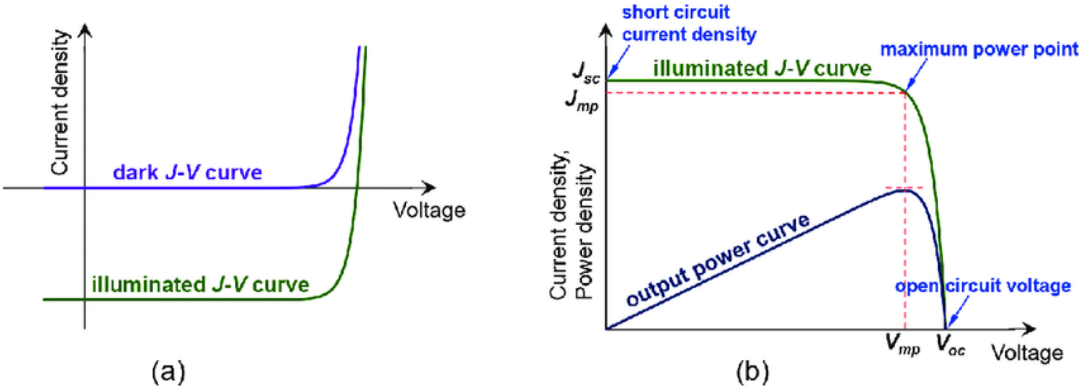

Figure 3.14: Typical J-V curves under light and dark conditions [17]

Summary

In this chapter, the methodology adopted to assemble the soiling station has been described to achieve the goals and objectives which were mentioned in chapter 1. The methodology describes the design of the soiling chamber and drawings of different sides of the chamber. Then it discusses the electrical wiring and relay control mechanism which helped to achieve the automation of the soiling station. The working and specifications of different instruments used in the soiling station have been explained. Moreover, the integration of these instruments and their role in achieving the daily outdoor soil cycle have been discussed. The simulation of the daily outdoor soil cycle has been discussed. In the outdoor cycle, in the morning time dew falls on modules then soil sticks on the module. After that during noontime, modules get heated and in the evening time, it gets cooled again. The same outdoor cycle has been simulated in the soiling chamber.

References

[1] Hammond Z, Curtis T, Simpson L, Tamizhmani G. Design Advancement of an Indoor Soil Deposition Chamber: A Road to Standardization. Conf. Rec. IEEE Photovolt. Spec. Conf., Institute of Electrical and Electronics Engineers Inc.; 2019, p. 3263–8. https://doi.org/10.1109/PVSC40753.2019.8981244.

[2] LED Flood Lights - Everything You Need To Know - The Lighting Outlet, https://thelightingoutlet.com.au/blogs/news/everything-you-need-to-know-on-led-floodlights (accessed May 31, 2021).

[3] ACS175246 – INGCO Silent and Oil-Free Air compressor – Safecon Enterprises Ltd, https://safecon.co.ke/product/acs175246-ingco-silent-and-oil-free-air-compressor/ (accessed May 31, 2021).

[4] HTG3535CH datasheet - Relative Humidity AND Temperature Module, https://www.digchip.com/datasheets/parts/datasheet/816/HTG3535CH.php (accessed May 31, 2021).

[5] XH-W3001 TEMPERATURE CONTROL THERMOSTAT, https://uamper.com/products/datasheet/XH-W3001-230.pdf (accessed May 31, 2021).

[6] TEC1-12705 Cooler Datasheet pdf - Thermoelectric Cooler. Equivalent, Catalog, https://datasheetspdf.com/pdf/634367/HB/TEC1-12705/1 (accessed May 31, 2021).

[7] CCM5D Datasheet, http://images.100y.com.tw/pdf_file/57-CCM5D.pdf (accessed May 31, 2021).

Chapter 4

Experimental Procedure

4.1 Materials

Lead Iodide (PbI_2, 99.9%), Methylammonium iodide (MAI, 99.9%), Cesium bromide (CsBr, 99.9%), polyvinyl acetate (PVAc), carbon black and graphite flakes were purchased from Sigma Aldrich. FTO glass, N-dimethylformamide (DMF, anhydrous 99.8%), dimethyl sulfoxide (DMSO, 99.8%), and chlorobenzene (CB, anhydrous 99.8%) were also purchased from Sigma-Aldrich. While Titanium (IV) isopropoxide (TTIP, 99.9%) and mesoporous Titania dioxide (Meso-TiO_2) were also purchased from Sigma Aldrich as well. All reagents were employed as received without further purification.

4.2 Characterizations

Using the Bruker, D8 Advanced with a scanning rate of 0.02^{o}/s and 2 in the range of 5^{o} and 70^{o}, the X-ray Diffraction (XRD) technique was performed to examine the structural makeup and crystal size of the perovskite films. A CuK radiation source (=154056) was produced at an excitation voltage of 25kV and a current of 40mA was employed for the XRD. Utilizing the UV-Vis NIR Spectrophotometer UV-3600 Plus, it was possible to examine the optical characteristics of the perovskite absorber layer. The samples' absorbance was determined to be between 350 and 1100 nm.PL (photoluminescence) was used for the emission spectra at an excitation peak of 380nm. iHR-320 spectrophotometer of Horiba scientific was used in the range of 389nm to 1100nmT^{o} explore the relationship between the functional group and the current Species, FT-IR spectra of produced thin films were obtained using FT-IR spectrum 100 PerkinElmer. For more accurate analysis, transmittance data of an extremely thin layer of absorber layer were obtained in the range of 600–4000cm^{-1} with a scan rate of 2cm^{-1}.

SEM and AFM, two distinct pieces of equipment, were used for the morphology study. Using scanning electron microscopy (SEM), the thin films' shape and grain size analysis were examined (TESCAN-VEGA-3). With an accelerating voltage of 15.0–10.0kV and a field magnification of 5um–500 nm, SEM pictures were studied. Atomic force microscopy was used to examine the surface shape and roughness (AFM). In static mode, a Nanosurf FlexAFM Version 5 was employed.

4.3 Fabrication of the Electrodes

Fabrication of the electrodes is done in three different stages:

4.3.1 Electron transport layer synthesis

To prepare the C-TiO_2 precursor, two different solutions were prepared. For solution 1, 2.53 ml of IPA was taken and added into 570ul of TTIP, and solution 1 was prepared. For solution 2, 28ul of 2M HCL was taken and added to 2.53 ml of IPA, and solution 2 was made. While stirring, solution 2 was added drop by drop into solution 1 very carefully and the precursor solution of C-TiO_2 was stirred for 30 minutes at room temperature on the hot plate.

For meso-TiO_2, a standard meso-TiO_2 paste was diluted with ethanol into 1:8 and a precursor solution was stirred for 30 minutes at room temperature on the hot plate.

4.3.2 Preparation of Absorber layer precursor solution

The $MAPbI_3$ precursor solution was prepared by dissolving 461mg of PbI_2 and 159mg CH_3NH_3I (1:1M ratio) in 700ul of DMF and 300ul of DMSO solution. The $MA_{1-x}Cs_xPb\,(I_yBr_{1-y})_3$ precursor solution with x=0.10 was obtained by dissolving 461mg of PbI_2, 143.78mg of CH_3NH_3I, and 21.2mg of CsBr (1:1M ratio) in 700ul DMF and 300ul DMSO solution. All perovskite solutions were heated at 70C for 12 hours inside the glove box filled with nitrogen gas before the film deposition, the whole process is shown in figure 4.1.

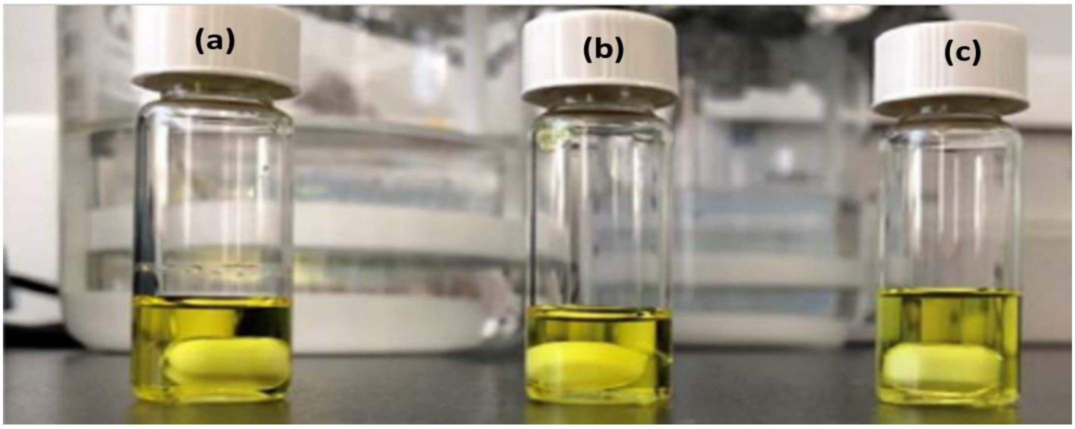

Figure 4.1: Preparation of the Perovskite film at different CsBr doping concentrations, (a) x=0.00, (b) x=0.09, (c) x=0.15

4.3.3 Preparation of the Carbon Counter Electrode

Carbon paste was prepared before the carbon counter electrode. The components in carbon paste were 600mg carbon black powder and 400mg graphite in 10ml of chlorobenzene solvent. The PVAc in the paste acted as a binder. For the binder dispersion preparation, took 1g of PVAc in 11ml of chlorobenzene solvent and stirred it on the hot plate at room temperature for 24 hours. Now add 4ml of this binder dispersion into the as-prepared carbon paste and now ball-milled this carbon paste including the binder dispersion for 24 hours, as shown in figure 4.2.

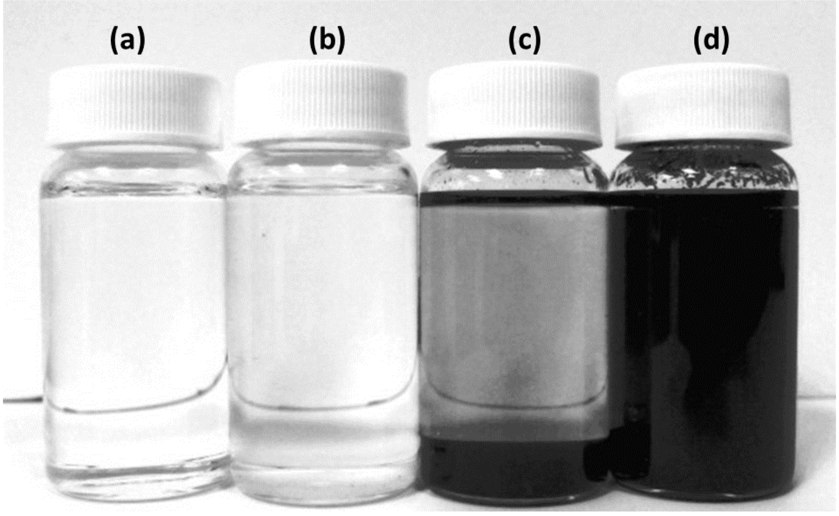

Figure 4.2: Preparation of the carbon electrode, (a) 11ml of CB, (b) binder solution, (c) carbon and graphite flakes in CB, (d) carbon and graphite flakes in CB+ binder dispersion

4.4 Solar Cell Fabrication

With a device structure of FTO/TiO_2/Meso-TiO_2/$MA_{1-x}Cs_xPb$ $(I_yBr_{1-y})_3$/Carbon powder/Counter FTO, PSCs were created. To clean the etched FTO-coated glass substrate, ultrasonication was used in deionized water, isopropanol, acetone, and isopropanol for fifteen min each at 55^{o}C. Spin-coating was used to deposit a blocking layer of C-TiO_2 (c-bl-TiO_2) on the FTO substrate for the 30s at a speed of 3000rpm. The compact FTO/bl-TiO_2 layer was then heated for 5 minutes at 125^{o}C. Following this, the sample was dried for 30 minutes at 450^{o}C, and the substrate was cooled gradually to room temperature. The mesoporous TiO_2 (mp-TiO_2) was further spin-coated with dilute TiO_2 pastes (20 nm -sized particles) in ethanol (1:7 weight ratio) at 3500 rpm for the 20s and heated this layer at 125Co for 5 min. This layer was sintered at 500^{o}C for 30 min and then cool it at room temperature. The perovskite solutions $MA_{1-x}Cs_xPb$ $(I_yBr_{1-y})_3$, x=0, 0.09 and 0.15) were then spin-coated onto FTO/c-bl-TiO_2/ Meso-TiO_2 substrate at 2000rpm for 30s. Chlorobenzene was dripped on the rotating substrate as the anti-solvent 10s before the finishing of the spin coating. The samples were annealed on a hot plate at 100^{o}C for 20 min to produce uniform $MA_{1-x}Cs_xPb$ $(I_yBr_{1-y})_3$ films. Carbon CE electrodes were deposited by using the doctor blading. Kapton tape was used for the groove pasting of the carbon layer. The thickness of the carbon layer was optimized by using the Kapton tape. Doctor blade the carbon layer after making the groove by using the Kapton tape, shown in figure 1, and air dry it for 10 minutes. After this annealed this carbon layer on the hot plate at 70^{o}C for 20 minutes in an open environment at 50% RH, as shown in figure 4.3. The whole-cell fabrication of the PSCs is shown in figure 4.4.

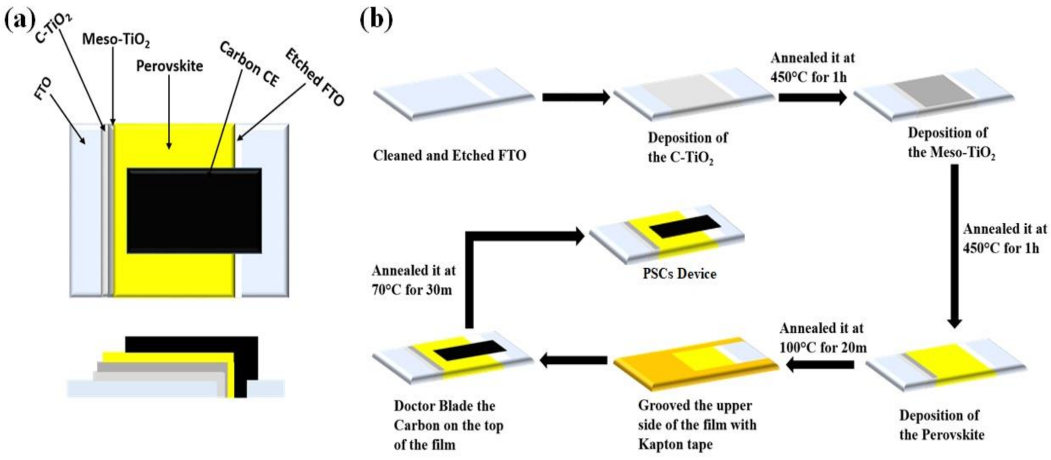

Figure 4.3: Fabrication of PSCs by using one-step spin coating in the dry glove box, (a) Structure of the PSCs by using Carbon CE, (b) Step by step methodology for the fabrication of the PSCs

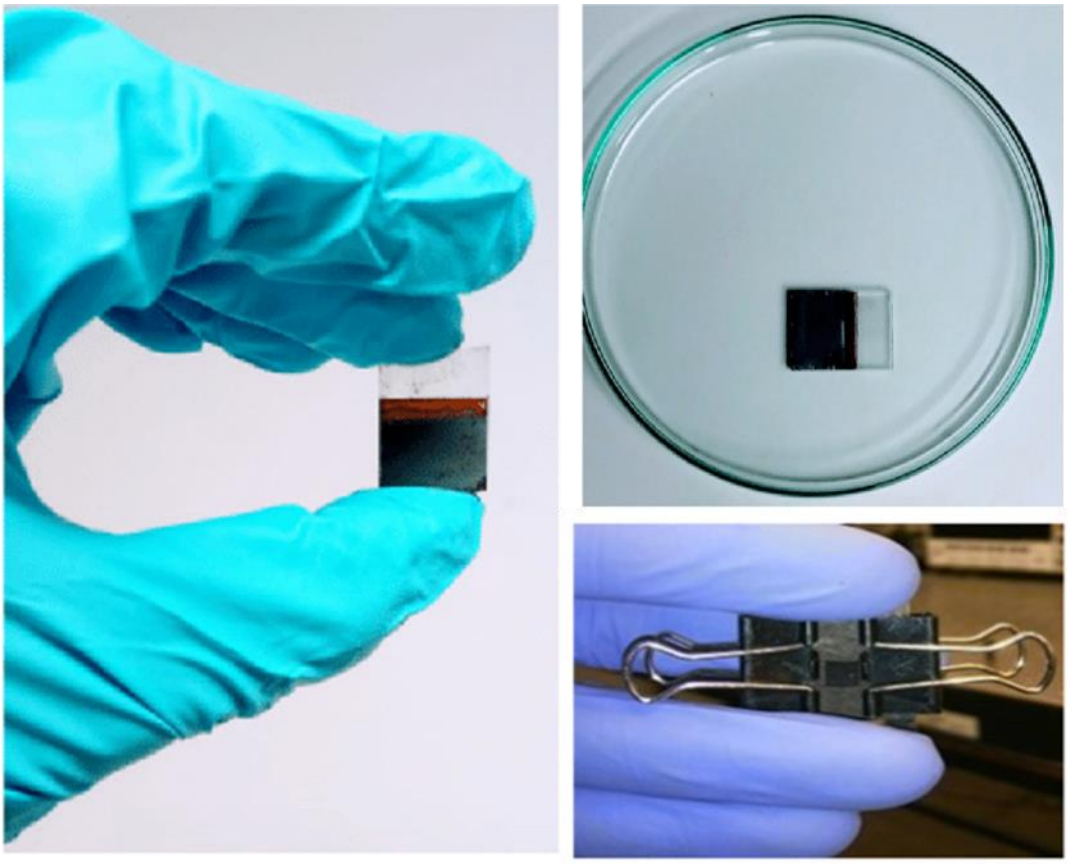

Figure 4.4: Structure of the perovskite solar cells fabricated in the lab

4.5 Characterization of solar cells

Characterization techniques were carried out after the successful fabrication of the perovskite film at different CsBr concentrations. For the structural investigation and crystal size analysis of the perovskite films, XRD and FT-IR were used. To study the optical properties of the perovskite absorber layer, UV-Vis was used. The absorbance of the samples was measured in the range of 350nm to 1100nm. PL (photoluminescence) was used for the emission spectra at different CsBr concentrations. To measure the thickness of the layers optical profilometry was used. For the Morphology analysis, two different equipment were used SEM and AFM. The morphology and grain size analysis of the thin films was observed by using scanning electron microscopy (SEM). The surface topography and roughness were investigated using the atomic force microscopy technique (AFM). The contact angle was used to measure the hydrophobicity of the different layers. For the electrical properties of the PSC IV simulator was used.

Summary

The experimental setup involves the preparation of the electron transport layers C-TiO_2 and meso-TiO_2 precursors at room temperature. The C-TiO_2 was prepared by using the TTIP precursor material with IPA. Meso-TiO_2 was prepared by diluting a standard meso-TiO_2 paste diluted with ethanol into 1:8 and the precursor solution was stirred for 30 minutes at room temperature on the hot plate. After that, a much simpler method was used to fabricate Cs and Br co-doped perovskite films from a solution of MAI, PbI_2, and CsBr in a mixed solvent containing DMF and DMSO by spin coating in a dry glove box at a humidity level of less than 10%. A molar ratio of CsBr: MAI: PbI_2 is 0:1:1, 0.09:0.91:1, 0.15:0.85:1 was used to prepare the best quality layer. Carbon was used for the preparation of the hole transport layer. The components in carbon paste were 600mg carbon black powder and 400mg graphite in 10ml of chlorobenzene solvent. Carbon counter electrodes were deposited by using the doctor blade technique on the surface of the perovskite film. Low-temperature perovskite solar cells device structure is used for the fabrication of the full device. A good quality layer with improved efficiency and stability was obtained as compared to the standard layer. The perovskite films were characterized by using UV-Vis, XRD, PL, AFM, SEM, EDS, and contact angle to check the incorporation of the CsBr in the film. The electrical parameters of the whole device testing were done by using an IV simulator.

Chapter 5

Results and Discussion

5.1 Structural Properties

In structural properties two different characterization techniques were performed:

- X-Ray Diffraction
- Fourier transform Infrared Region

5.1.1 X-Ray Diffraction

We gathered the X-ray diffraction (XRD) waveforms of the perovskite films with different doping densities, as shown in Fig. 1a, to examine the impact of CsBr doping on the crystallinity of perovskite films. As seen in Fig. 5.1(a), all samples display the typical perovskite tetragonal phase, with diffraction peaks at 14.16°, 20.06°, 23.54°, 24.55°, 28.50°, 31.95°, and 40.72°, respectively, corresponding to the (110), (112), (211), (202), (220), (310), (312), and (224) crystal planes[1]. There is relatively little difference between the locations of the diffraction peaks from perovskite films with different levels of doping. For a low Cs doping level, this minor modification might be the result of a lattice strain or distortion in the $MAPbI_3$ perovskite. The lack of extra peaks in any of the XRD patterns beyond those for the plain perovskite film ($x = 0$) suggests that the CsBr doping level in our samples is too low to introduce a new phase. Additionally, as the Cs content rises, the breadth of the diffraction peaks is shown to be slightly different from the control sample, indicating a reduction in the size of crystal domains as a result of the integration of Cs, as shown in figure 5.1(b). Further, we note that the crystallinity of perovskite improves with the incorporation of Cs, which was shown by the intensity change in the (110) and 220 planes the peak intensity of (110) and (220) planes increase significantly for $x=0.09$ films while it starts decreasing by further increasing the Cs content ($x=0.15$)[2][3].

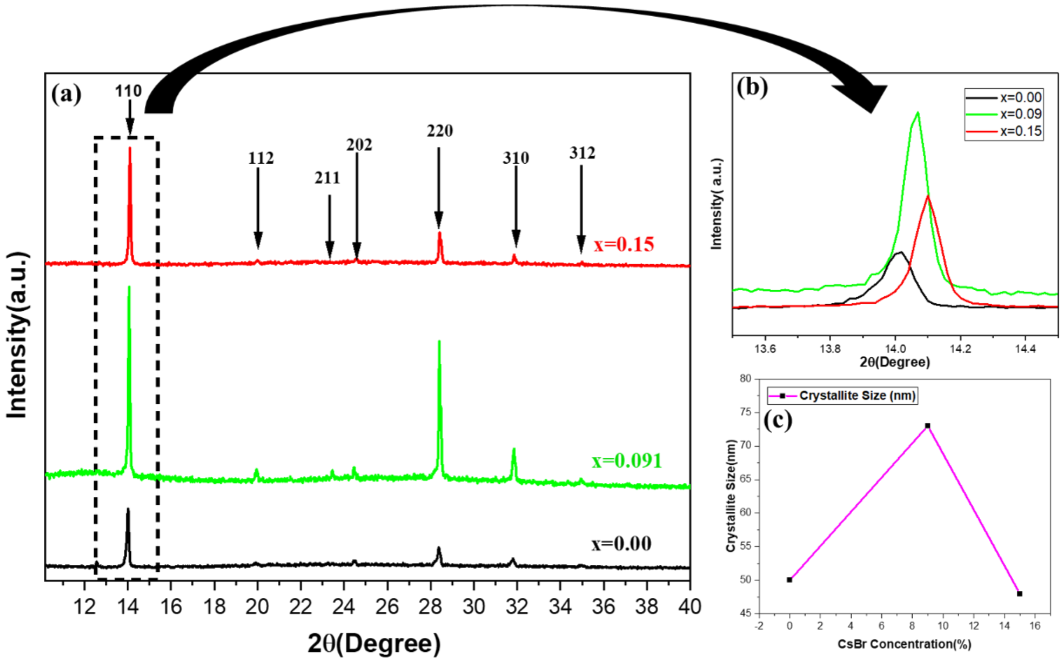

Figure 5.1: X-ray diffraction (XRD) patterns of the perovskite films, (a) 2-theta values of CsBr concentration in $MAPbI_3$, (b) XRD peak magnified at 14.0°

We determined the crystallite size and full-width half maximum (FWHM) for x=0, 0.09, and 0.15, and we found that the FWHM for x=0.09 is the smallest (0.095), indicating the highest crystallinity and the highest peak of the perovskite phase in the (110) plane [4]. Thus, using the Scherrer formula and the diffraction peak at 14.02, we can determine the size of the perovskite crystal grain.:

$$D = \frac{0.9\lambda}{\beta cos\theta} \qquad \text{(Eq. 5.1)}$$

k is the X-ray wavelength (0.154 nm), D is the grain size, b is the full width at half maximum (FWHM) of the (110) peak, and h is the Bragg angle, respectively [2]. Figure 5.1 presents the computed outcomes (c). Since CsBr doping increases grain size in the perovskite film to x=0.09, the larger the perovskite grain size will be the higher the CsBr doping level. However, at a certain concentration, crystallite size begins to decline because, while crystallite size improves as intensity improves, it begins to decline as FWHM increases. Additionally, we created perovskite films with Cs concentrations above 15%. The films, however, were found to be extremely rough and uneven, with low purity and a large density of pinholes.

5.1.2 Fourier transform Infrared Region

As CsBr is present in $MAPbI_3$ crystals, FT-IR was used to determine the strength and orientation of known chemical bonds as well as to look for any changes in bond locations. FT-IR is a potent method that uses IR absorption to pinpoint the bonds in an organic molecule. The method is especially helpful in identifying specific signature peaks when the orientation of bonds in complicated structures like perovskites changes as a result of the presence of external stimuli. The $MA_{1-x}Cs_xPb\ (I_yBr_{1-y})_3$ perovskite's FT-IR spectra were taken at room temperature in film form, as shown in Figure 5.2 (a). N-H, C-H, and CH_3-NH_3 peaks have been accurately recreated in several investigations that report vibrational spectroscopic observations of typical $MAPbX_3$ perovskites. As illustrated in figure 5.2, in our situation, with x=0.00 Cs doping, we see four distinct peaks of $MAPbI_3$ precursor at 900 cm^{-1}, 1500 cm^{-1}, and 3180 cm^{-1} (a). The NH^{3+} ion's N-H stretch is represented by the peak at 3150 cm^{-1}, which exhibits a minor doublet structure and is likely indicative of both symmetric and asymmetric NH^{3+} stretching. The CH^3-NH^{3+} peak is located at 900 cm^{-1}, and the ammonium bond bending peak is located at 1500 cm^{-1}. The peak near 3180 cm^{-1} is replaced by two distinct peaks (3180 cm^{-1} and 3116 cm^{-1}), resulting in a little variation of the CH3-NH3 structure, and the peaks are extremely similar to pure $MAPbI^3$ peaks with minor variations as the Cs doping advanced into the $MAPbI^3$ structure. This demonstrates that whereas the inorganic homolog is stable, the local environment of the methylammonium group is first altered by the presence of Cs. The double peaks of 3180 cm^{-1} and 3116 cm^{-1} remained noticeable as the concentration of Cs rose, reaching their highest intensity around x=0.09. The strength of the peaks at 3180 cm^{-1} and 3116 cm^{-1} gradually decreases at x=0.15. Regarding the peaks, they begin to intensify at 1500 cm^{-1}, but at x=0.15, not before. If we add more CsBr, the CsBr is drastically reduced till it practically disappears. However, there is little to no impact on the 900cm^{-1} peak. As a result, the structure percolates when Cs levels rise over a particular threshold of x=0.09, changing the conductivity. It is still unclear, though, whether the doped Cs force the development of a new structure or merely cause a shift in the electrical structure of the area[32].

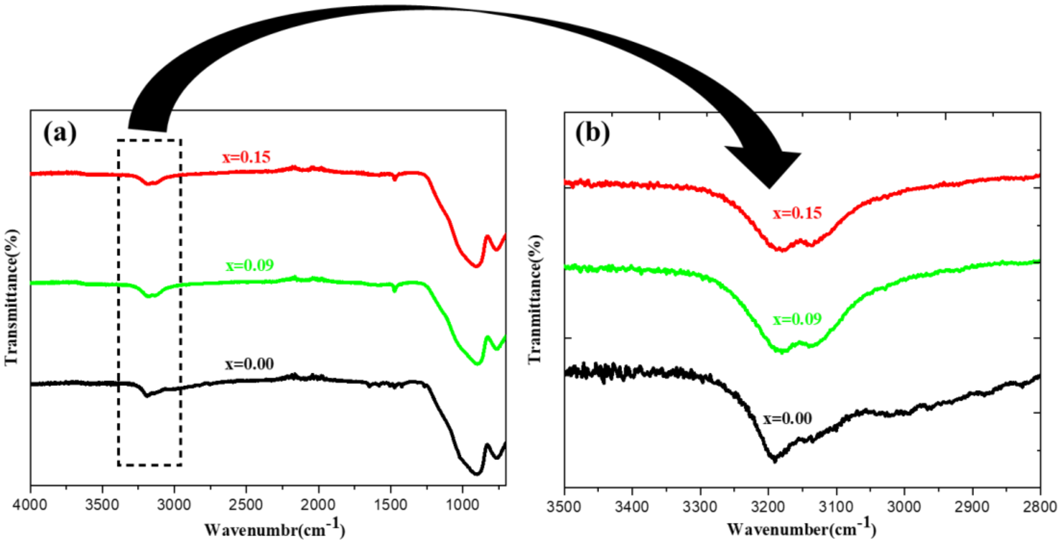

Figure 5.2: FT-IR spectra for Different CsBr ration in $MAPbI_3$, (b) Magnified at 3180cm^{-1}

5.2 Optical Properties

In optical properties two different characterization techniques were performed:

- UV- vis Spectroscopy
- Photoluminescence

5.2.1 UV- vis Spectroscopy

Figure 53 displays the UV/vis absorption spectra for pure $MAPbI_3$ and various CsBr concentrations combined with $MAPbI_3$ (a). A large absorption peak was seen between 450 and 790 nm[5], for the pure $MAPbI_3$ perovskite absorber layer, which was attributed to the entire production of $MAPbI_3$ perovskite as shown by XRD patterns (Fig. 2(a)). A further rise in the Cs concentration causes the bandgap, which is a result of the constructive crystal lattice, to widen, and shifts the absorption edge towards a shorter wavelength area. The value of E_g was determined using the method described by A. B. Morphyen in Ref.[6], which initially calculates the absorption coefficient and then, taking the values of α found and considering that for direct gap materials the relationship $(\alpha h\nu)^2 = A\ (h_\nu - E_g)$ is fulfilled, the value of Eg can be determined from the intercept with the hν axis that results from extrapolating the linear region of the curve $(\alpha h\nu)^2$ vs hν[7], figure 5.3(c-e).

The values of optical band gap (E_g) obtained for the perovskite was almost similar (1.57 eV) for pure and with increasing the concentration of CsBr, x=0.00, 0.09, and 0.15 in $Cs_x MA_{(1-x)} Pb (I_yBr_{1-y})_3$ the bandgap also increased in the range of 1.58,1.61 and 162 eV implying that optical band gap can be easily tuned by controlling the amount of CsBr in perovskite, as shown in figure 5.3(b). Perovskite materials that have low bandgap can absorb lower-energy photons to generate more electron-hole pairs. However, V_{oc}, in this case, is limited by the bandgap of the semiconductor, the open circuit being normally less than the band gap. Photo generated electron-hole pair is separated by an electric field in perovskite films, electron and hole move out of this region under the acceleration induced by an electric field, so that high V_{oc} will accelerate separation progress of electron-hole pair. Photo generated electron-hole pair, which is collected by two electrodes of photovoltaic devices, is an effective electron and hole, so we need to tune the perovskite bandgap to generate a more effective electron and hole.

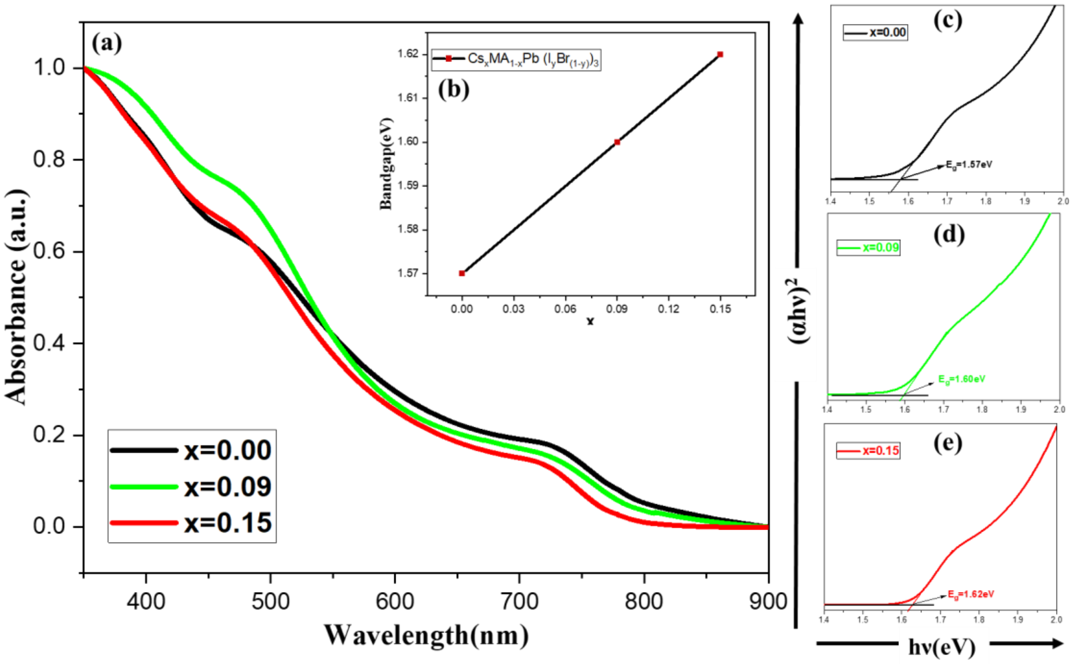

Figure 5.3: (a)Absorption Curves for different x=0.00, 0.03, 0.06, 0.09, 0.12 and 0.15, (b) Band gap of the perovskite film at different CsBr doping concentrations, (e-e) Tauc plot at different CsBr doping concentrations

5.2.2 Photoluminescence

The photophysical properties of the $MA_{1-x}Cs_xPb(I_yBr_{1-y})_3$ nanocrystals were evaluated using absorption and steady-state photoluminescence (PL) measurements with the gradual addition of Cs^+ and the corresponding results are exemplified in figure 5.4(a). From the PL study, it is witnessed that the emission maxima ($\lambda_{em\ max}$) of the $MA_{1-x}Cs_xPb$ (I_yBr_{1-y}) nanocrystals can be adjusted in the range of 765–760nm with a fixed excitation peak at 380nm[8]. PL intensity of $MA_{1-x}Cs_xPb$ $(I_yBr_{1-y})_3$ perovskite thin films increased continuously for a small amount of Cs^+ incorporation, however, it decreased with larger amounts of Cs^+ incorporation. The enhanced PL intensity with small Cs^+ incorporation due to internal defect reduction of $MA_{1-x}Cs_xPb$ $(I_yBr_{1-y})_3$ (x = 0–0.09) perovskite. When excited at a single wavelength, the less defective perovskite could generate more electron-hole and photons through radiative recombination of photogenerated charge carriers, which enhance the PL intensity[9]. Less defect also increases carrier-diffusion lengths and fluoresce lifetime of perovskite thin films. The intensity of the PL peak of the cesium-doped perovskite film is higher than that of the pristine perovskite film, which indicates decreased surface-trap states (related to non-radiative PL recombination) and increased perovskite crystallinity (consistent with the SEM results) a Larger amount of Cs^+ incorporation result in PL intensity decrease, an increase of $MA_{1-x}Cs_xPb$ $(I_yBr_{1-y})_3$ (x = 0.09–0.15) perovskite internal defect result in the decrease of charge carrier lifetime[5][10], as shown in figure 5.4(a).

To gain further insights into film quality after the incorporation of CsBr into the perovskite precursor, electronic disorder below the optical band gap known as Urbach energy was calculated by linear fitting ln(α) versus h_γ profile using the relation $\alpha = \alpha^0$ exp (E/E_u), where α is the absorption coefficient, E $(=h_\gamma)$ is the photon energy, and E_u is the Urbach energy[11][12]. As shown in Figures 5.4 (b) and (c), the control sample has Eu ~216 meV, where CsBr (x=0.09) showed a reduced value of 152meV. The observed reduction in the Urbach energy is an indication of the reduced density of trap sites. These findings are in line with the steady-state photoluminescence (PL) study of perovskite films, as shown in figure 5.4 (a). It was found that the PL intensity for the CsBr (x=0.09) film was higher compared to that for the control film (x=0.00). This indicates reduced non-radiative recombination loss due to possible passivation of the surface and bulk-related defects. There is no noticeable peak shift in the PL spectra after the treatment[13].

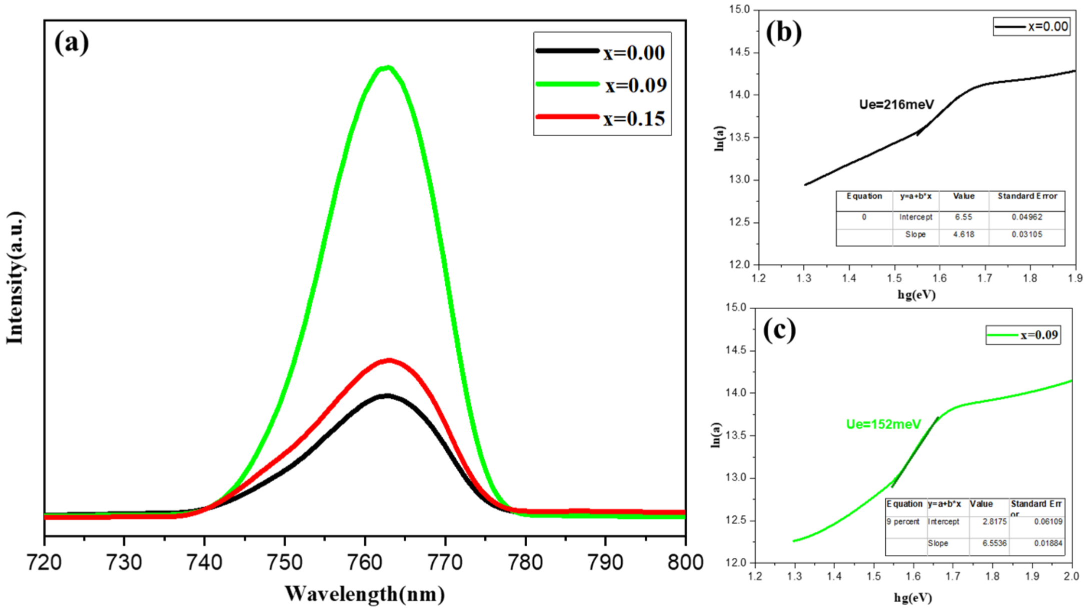

Figure 5.4: (a) Photoluminescence spectra of Cs$_x$MA$_{1-x}$PbI$_3$ thin films, (b) Estimation of Urbach energy for x=0.00, (b) Estimation of Urbach energy for x=0.09

5.3 Morphological Properties

In morphological properties three different characterization techniques were performed:

- Scanning Electron Microscopy
- Atomic Force Microscopy
- Contact Angle

5.3.1 Scanning Electron Microscopy

Grain boundaries (GBs) in perovskite film are mainly responsible for non-radiative recombination and also promote trap-assisted charge carrier recombination because of the existence of numerous defects at GBs. In some studies, it was found that the process of ion migration tends to dominate at GBs in MAPbI$_3$ based perovskites rather than in the grain interiors. Recently, Xing *et al*. studied the ion migration properties of MAPbI$_3$ films with different grain sizes[14] and found that an increase in grain size leads to an increase in E_a of ionic migration. The E_a for large grain film was much higher (E_a = 0.50 eV) as compared to the smaller grain film (E_a = 0.27 eV) in the dark condition. This increased E_a suggests a higher energy barrier. for the migration of ions. The aforementioned studies reveal that the engineering of GBs may help in suppressing the ion migration and hysteresis in PSCs. Since then, several research groups have established that increasing grain size causes a decrease in GBs[15][16], which assists in the formation of pinholes and defect-free film promoting negligible hysteresis[17]. This result is further confirmed by scanning electron microscopy (SEM), figure 5.5 shows the top view of scanning electron microscope (SEM) images for mixed cation perovskite films prepared from Cs concentrations of x=0.00, 0.09, and 0.15. It is clear from the surface image of perovskite films that the films have grown with large grains, full coverage of substrates, and no visible pinholes observed. GBs minimized when the CsBr doping level is x=0.09 (figure 5.5(b)). The grains with a size of 50-300 nm are close-packed with clear grain boundaries. Also, it is clear from the EDS spectra that for the undoped samples there was no peak for the Cs^+ and Br^- but the prominent peaks can be seen in the EDS spectra for doped samples when the concentration of the cesium bromide is increased. Nevertheless, as shown in figure 5.5(c), when the Cs+ concentration is further increased to 15%, the grain size is slightly decreased and CsBr particle agglomeration can be observed. This agglomeration cites may increase the surface roughness.

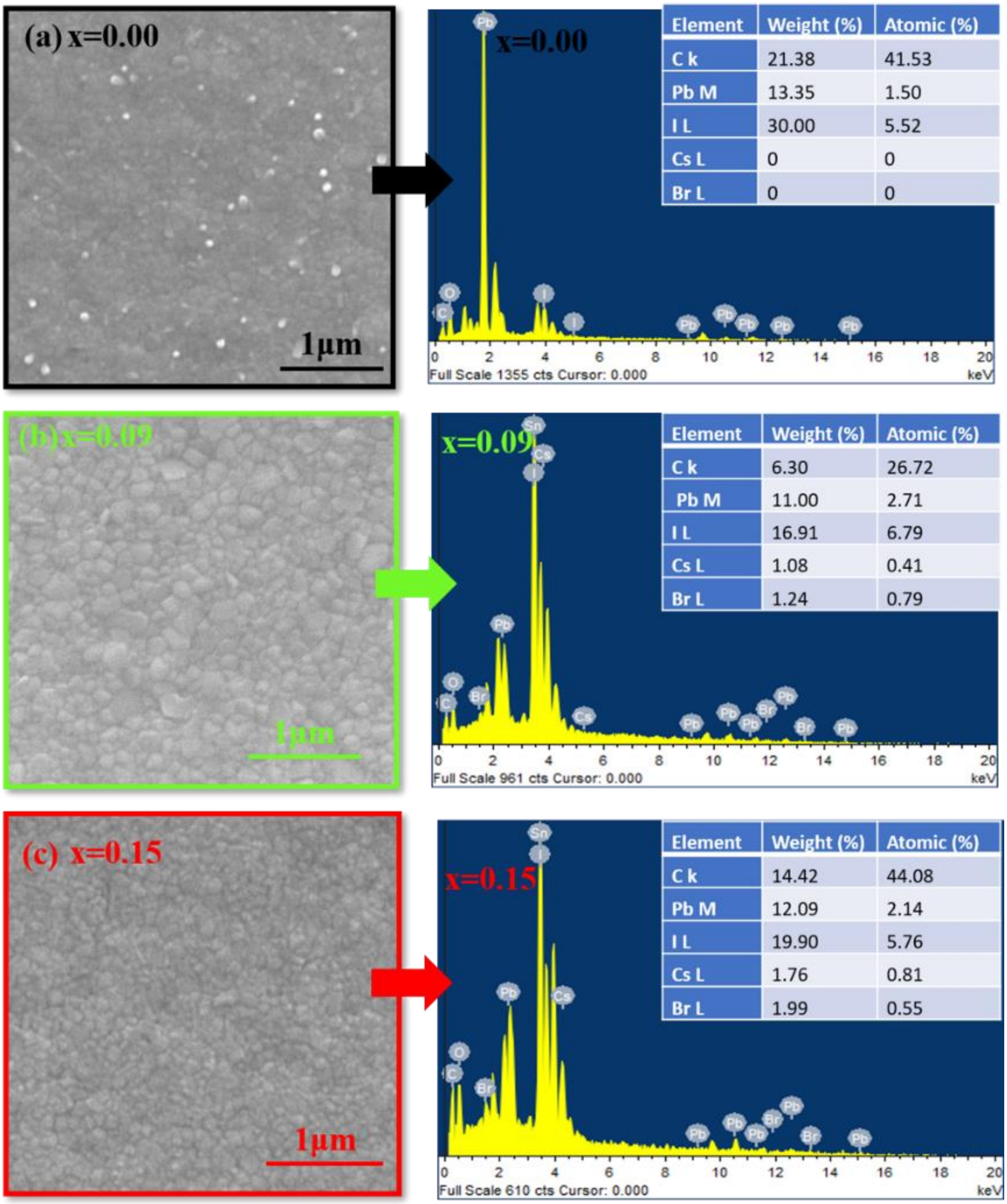

Element	Weight (%)	Atomic (%)
C k	21.38	41.53
Pb M	13.35	1.50
I L	30.00	5.52
Cs L	0	0
Br L	0	0

Element	Weight (%)	Atomic (%)
C k	6.30	26.72
Pb M	11.00	2.71
I L	16.91	6.79
Cs L	1.08	0.41
Br L	1.24	0.79

Element	Weight (%)	Atomic (%)
C k	14.42	44.08
Pb M	12.09	2.14
I L	19.90	5.76
Cs L	1.76	0.81
Br L	1.99	0.55

Figure 5.5: Top view of SEM and EDS for different CsBr doping concentrations, (a) x=0.00, (b) x=0.09, and (c) x=0.15

5.3.2 Atomic Force Microscopy

This can be seen from the AFM, as shown in figure 5.7, when the concentration of the Cs^+ and Br^- is low the surface roughness and root mean square roughness (R_{rms}) is high but as soon as the doping concentration of the Cs^+ and Br^- is starts increasing this R_{rms} value starts decreasing from 60nm for undoped samples to 10nm for doped samples(x=0.09). It simply means that with increasing the doping concentration the GBs starts increasing and overall a smoother perovskite absorber layer is produced. With the smaller number of the GBs, charge transfer is enhanced, and as a result cell performance is increased. But after a certain level of CsBr doping concentration (x=0.15), the agglomeration is started with the increase in the R_{rms} value of 17nm, and film quality is deteriorating.

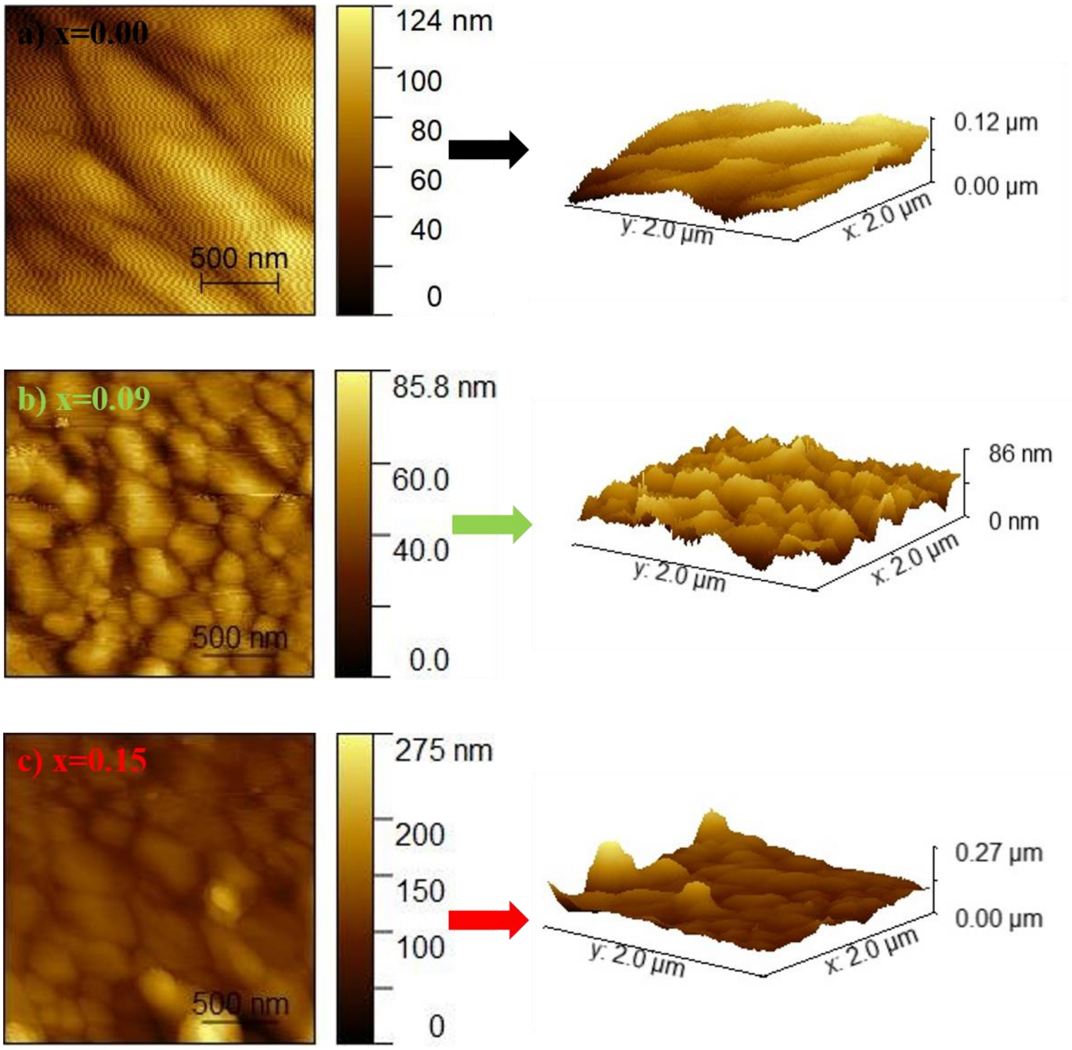

Figure 5.6: AFM results at different CsBr doping concentrations, a)x=0.00, b)x=0.09,c)x=0.15

5.3.3 Contact Angle

PL characterization was performed to check charge carrier transfer and extraction behavior at the surface of the perovskite/Carbon electrode at different CsBr concentrations. Photoluminescence spectra show a perovskite luminescence peak at 760nm, demonstrated in figure 5.7 (a). In the presence of a Carbon electrode, photoluminescence was substantially quenched, indicating charge transfer between CE and the perovskite photoactive layer[18]. It is interesting to note that photoluminescence quenching was even more extensive when doping concentration is increased ($x=0.09$) because at this doping concentration the perovskite absorber layer has fewer trap defect states and fewer GBs. However, when the doping concentration is further increased ($x=0.15$), the photoluminescence peak is starting increasing which means that the presence of trap defect states increases with the agglomeration at the surface of the film, and charge carrier transfer is hindered by the presence of this poor quality of the film and overall efficiency and stability of the device is compromised[18]. The water contact angle was measured to further investigate the role of carbon electrodes in increasing the stability of the PSCs devices[19]. The water contact angle was measured on the (a) Cesium doped absorber layers and (b) Cesium doped absorber layers with carbon as a counter electrode, to check the effect of the humidity on the cesium doping and with carbon as a counter electrode. As demonstrated in figure 5.7(b-g), as the CsBr doping level is increased the water contact angle is increased due to the more compact film morphology. On the other hand, when the carbon is deposited on the perovskite films, they became more hydrophobic and with a more compact structure and larger contact angle to the water, the carbon/perovskite layer on top of the cell will offer better protection against moisture, and eventually, improves stability[19].

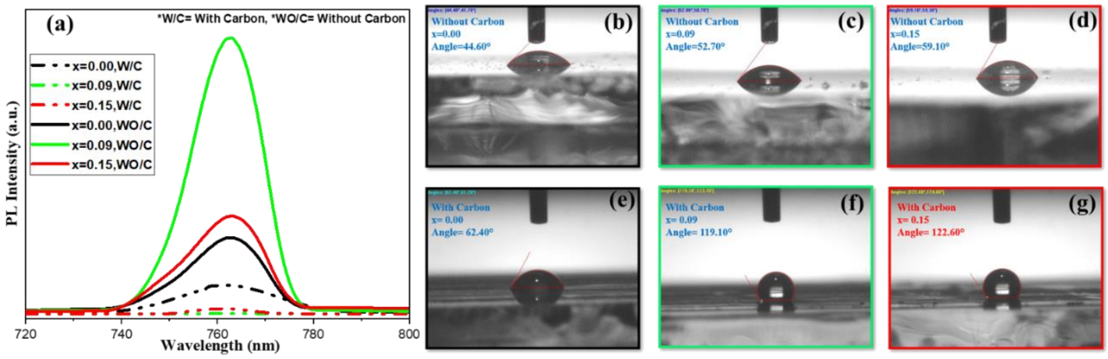

Figure 5.7: Carbon counter Electrode, a) PL results with Carbon and without carbon, b),c),d), Perovskite absorber layer contact angle with CsBr doping at x=0.00,x=0.09,x=0.15, e),f),g) Perovskite absorber layer contact angle with Carbon as a counter electrode at different concentration of CsBr (x=0.00, x=0.09, x=0.15)

5.4 Electrical Properties

In morphological properties three different characterization techniques were performed:

5.4.1 IV-Simulator

The energy-level diagram of C-PSCs is shown in Fig. 10(a). Because of the ambipolar perovskite and energy-level alignment, the holes can be captured by the carbon electrode and sent to the external circuit while the electrons can be efficiently injected into the conductive band of TiO_2. Fig. 10 displays the photocurrent-voltage (J-V) curves of the solar cells with carbon electrodes under AM 1.5 illumination of 100 mW/cm2 in order to assess the impact of CEs on the performance of the solar cells (b). Table 1 lists the specific photovoltaic parameters. As is well known, charge transport and transfer in solar cells heavily rely on the interface contact between perovskite and carbon CE. Poor interfacial contact between the perovskite layer and the graphite flakes is mostly to blame for the poor performance of the cell with CE[20].

Table 5.1: Performance summary for perovskite solar cells with different CsBr doping concentrations

X	V_{mp} (V)	I_{mp} (A)	V_{oc} (V)	J_{sc} (mA/cm^2)	FF	η (%)
0.00	0.306	5.07	0.530	9.56	0.29	1.55
0.09	0.542	11.13	0.659	18.53	0.44	5.27
0.15	0.368	8.41	0.639	14.13	0.30	3.09

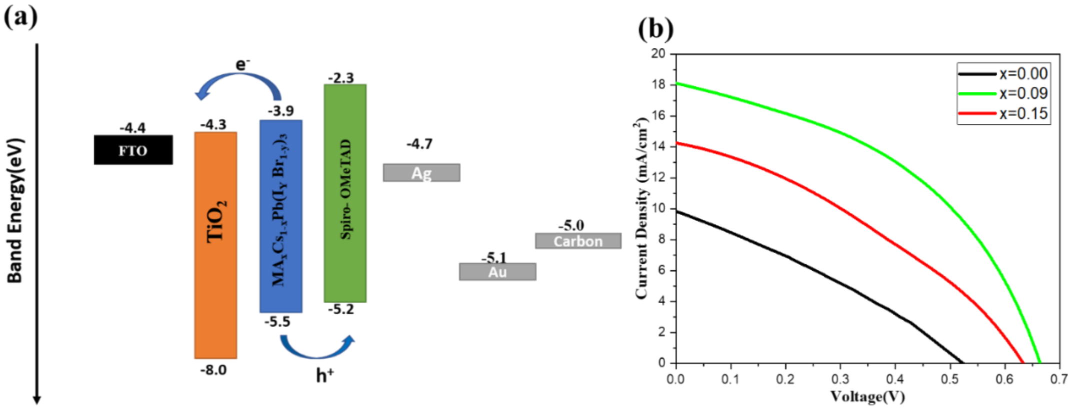

Figure 5. 8: a) Band alignment of PSCS, b) J-V results with different CsBr doping concentrations

Figure 5.8(b) displays the current density-voltage (J-V) curves of the best-performing cells with various Cs^+ and Br^- ratios. These devices were made with the architecture of FTO/C-TiO_2/mp-TiO_2/$MA_{1-x}Cs_x Pb(I_yBr_{1-y})_3$/Carbon (x = 0, 0.09, and 0.15). With an open-circuit voltage of 0.530 V, a high short-circuit current density of 9.56 mA cm^{-2}, and a fill factor of 0.29, the device made from pure $MAPbI_3$ perovskite film has a power conversion efficiency (PCE) of 1.55%. The Cs_+ ratio of x=0.09 yielded the highest PCE of 5.27 percent. When the Cs^+ ratio is raised further to x=0.15, the PCE declines by 3.09 percent. The decreased Jsc and Voc of the device with x=0.15 concentration, which may be related to the smaller grain sizes, were blamed for the device's decreased efficiency. Voc rises from 0.530 to 0.659 V, Jsc from 9.56 to 18.53 mA/cm^2, and FF from 0.29 to 0.44 when the CsBr doping level rises from x = 0 to x = 0.09. As shown in Table 5.2, the efficiency, as a result, rises from 1.55 percent for the undoped sample to 5.27 percent for the doped sample with x = 0.09. The XRD and SEM data (Figs. 5.1(a), 5.4) demonstrate that CsBr doping can result in a significant increase in the size of the perovskite crystal grains. Because of the lower area occupied by grain borders caused by the greater grain size, there will be fewer interface flaws that cause photogenerated carriers to recombine. Voc, Jsc, and FF will rise as a result of this enhancement. Br^- doping can aid in the growth of perovskite crystal grains, whereas Cs^+ doping cannot enlarge perovskite grains[21][22][23], Accordingly, we believe that replacing Br- with me- in $MAPbI_3$ is beneficial to the growth of perovskite crystal grains. The bandgap of the perovskite is blue-shifted following the CsBr doping, as shown in figure 5.8(b), which is consistent with the findings that only Cs or Br doping may broaden the bandgap of plain perovskite. This is another cause of the increase in Voc[21][22][24]. Another significant factor that contributes to the increase in Jsc as the CsBr doping level rises from x = 0 to x = 0.09 is the striking rise in optical absorption. The increased charge transport capabilities of the perovskite layer caused by the substitution of Br^- for I^- are responsible for the improved FF following CsBr doping[25]. The Voc, Jsc, and FF fall from 0.659 V, 18.53 mA/cm^2, and 0.44 to 0.639 V, 14.13 mA/cm2, and 0.30 percent, respectively, as the CsBr doping level rises from x = 0.09 to x = 0.15. The enlarged grain boundaries caused by the Cs-doping in both the XRD and SEM data (see figures 5.1(a) and 5.4) may increase the probability of charge carrier recombination and, as a result, reduce the photovoltaic current density[26][27].

Due to the aggregation of the Cs^+ and halide segregation, the smoothness of the perovskite absorber layer decreased as the Cs^+ and Br^- concentration increased. Due to the week-long contact between the perovskite and carbon interface, which raised shunt resistance and series resistance, the Jsc and Voc at x=0.15 decreased.

Summary

In this work, we studied the effect of different CsBr doping concentrations on the perovskite absorber layer. The introduction of Cs into the precursor solution would inevitably accelerate the film deposition rate which resulted in larger grain size and the film contained fewer grain boundaries. Due to this, the defects which are prominent like ion migration at the grain boundaries were reduced. Moreover, the defect state density was reduced which was evident in the PL spectra. The PSCs were fabricated by using the carbon CE after successfully optimizing the CsBr concentration at x=0.09. The high charge carrier mobility of the carbon counter enhanced the hole extraction from perovskite film and decreased the recombination in the device. We obtained the best performing perovskite device at x=0.09 with improved V_{oc}, J_{sc}, FF, and PCE. Voc rises from 0.530 to 0.659 V, Jsc from 9.56 to 18.53 mA/cm2, and FF from 0.29 to 0.44 when the CsBr doping level rises from x = 0.00 to x = 0.09. Additionally, for x = 0.09, the efficiency goes from 1.55 percent for the undoped sample to 5.27 percent for the doped sample. The hydrophobic and dense carbon CE layer also shields the perovskite film from outside moisture, which has a protective effect on it. Our finding suggests a new route for the investigation of inexpensive carbon-based materials and could be significant for the widespread industrial use of PSCs.

References

[1] Y. Fan, H. Qin, W. Ye, M. Liu, F. Huang, and D. Zhong, “Improving the stability of methylammonium lead iodide perovskite solar cells by cesium doping,” *Thin Solid Films*, vol. 667, no. September, pp. 40–47, 2018, DOI: 10.1016/j.tsf.2018.10.001.

[2] L. Y. Zhang, Y. Zhang, W. B. Guan, K. F. Wang, Z. X. Cheng, and Y. X. Wang, “Large enhanced conversion efficiency of perovskite solar cells by CsBr doping,” *J. Mater. Sci.*, vol. 52, no. 22, pp. 13203–13211, 2017, DOI: 10.1007/s10853-017-1429-3.

[3] Y. Zhao and K. Zhu, “Charge transport and recombination in perovskite (CH3NH 3)PbI3 sensitized TiO2 Solar Cells,” *J. Phys. Chem. Lett.*, vol. 4, no. 17, pp. 2880–2884, 2013, doi: 10.1021/jz401527q.

[4] T. Singh and T. Miyasaka, “Stabilizing the Efficiency Beyond 20% with a Mixed Cation Perovskite Solar Cell Fabricated in Ambient Air under Controlled Humidity,” *Adv. Energy Mater.*, vol. 8, no. 3, pp. 1–9, 2018, DOI: 10.1002/aenm.201700677.

[5] X.-C. Zhao, D.-X. Wu, L.-J. Yang, J. Tang, G.-Z. Yue, and P. Yang, “Cesium-Containing Methylammonium Lead Iodide Light Absorber for Planar Perovskite Solar Cells,” *J. Nanosci. Nanotechnol.*, vol. 20, no. 2, pp. 1008–1012, 2019, DOI: 10.1166/jnn.2020.16896.

[6] A. B. Murphy, “Band-gap determination from diffuse reflectance measurements of semiconductor films, and application to photoelectrochemical water-splitting,” *Sol. Energy Mater. Sol. Cells*, vol. 91, no. 14, pp. 1326–1337, Sep. 2007, DOI: 10.1016/J.SOLMAT.2007.05.005.

[7] G. Gordillo, L. C. Luis, J. P. Buitrago, and M. A. Reinoso, “Influence of the Concentration of Cs on the Properties of Thin Films of Cs X MA (1-X) PbI 3 to be used as Active Layer in Hybrid Solar Cells,” *2018 IEEE 7th World Conf. Photovolt. Energy Conversion, WCPEC 2018 - A Jt. Conf. 45th IEEE PVSC,*

28th PVSEC 34th EU PVSEC, pp. 2200–2203, 2018, DOI: 10.1109/PVSC.2018.8547601.

[8] S. Premkumar, K. Kundu, and S. Umapathy, "Impact of cesium in methylammonium lead bromide perovskites: Insights into the microstructures, stability, and photophysical properties," *Nanoscale*, vol. 11, no. 21, pp. 10292–10305, 2019, DOI: 10.1039/c9nr02733e.

[9] C. H. Ng *et al.*, "Tunable Open Circuit Voltage by Engineering Inorganic Cesium Lead Bromide/Iodide Perovskite Solar Cells," *Sci. Rep.*, vol. 8, no. 1, pp. 1–9, 2018, DOI: 10.1038/s41598-018-20228-0.

[10] A. Bahtiar, R. Yazibarahmah, A. Aprilia, and D. Hidayat, "Improved the performance and stability at high humidity of perovskite solar cells by mixed cesium-methylammonium cations," *Key Eng. Mater.*, vol. 860 KEM, pp. 9–14, 2020, DOI: 10.4028/www.scientific.net/KEM.860.9.

[11] Y. Zhang *et al.*, "High Efficiency (16.37%) of Cesium Bromide—Passivated All-Inorganic CsPbI2Br Perovskite Solar Cells," *Sol. RRL*, vol. 3, no. 11, pp. 1–8, 2019, DOI: 10.1002/solr.201900254.

[12] M. Ledinsky *et al.*, "Temperature Dependence of the Urbach Energy in Lead Iodide Perovskites," *J. Phys. Chem. Lett.*, vol. 10, no. 6, pp. 1368–1373, 2019, doi: 10.1021/acs.jpclett.9b00138.

[13] N. Ghimire *et al.*, "Mitigating Open-Circuit Voltage Loss in Pb-Sn Low-Bandgap Perovskite Solar Cells via Additive Engineering," *ACS Appl. Energy Mater.*, vol. 4, no. 2, pp. 1731–1742, 2021, DOI: 10.1021/acsaem.0c02895.

[14] J. Xing, Q. Wang, Q. Dong, Y. Yuan, Y. Fang, and J. Huang, "Ultrafast ion migration in hybrid perovskite polycrystalline thin films under light and suppression in single crystals," *Phys. Chem. Chem. Phys.*, vol. 18, no. 44, pp. 30484–30490, Nov. 2016, DOI: 10.1039/C6CP06496E.

[15] B. Yang *et al.*, "Perovskites: Enhancing Ion Migration in Grain Boundaries of

Hybrid Organic-Inorganic Perovskites by Chlorine (Adv. Funct. Mater. 26/2017)," *Adv. Funct. Mater.*, vol. 27, no. 26, Jul. 2017, DOI: 10.1002/ADFM.201770158.

[16] M. N. F. Hoque, R. He, J. Warzywoda, and Z. Fan, "Effects of Moisture-Based Grain Boundary Passivation on Cell Performance and Ionic Migration in Organic-Inorganic Halide Perovskite Solar Cells," *ACS Appl. Mater. Interfaces*, vol. 10, no. 36, pp. 30322–30329, Sep. 2018, DOI: 10.1021/ACSAMI.8B08981/SUPPL_FILE/AM8B08981_SI_001.PDF.

[17] R. Singh, S. Sandhu, H. Yadav, and J. J. Lee, "Stable Triple-Cation (Cs+-MA+-FA+) Perovskite Powder Formation under Ambient Conditions for Hysteresis-Free High-Efficiency Solar Cells," *ACS Appl. Mater. Interfaces*, vol. 11, no. 33, pp. 29941–29949, Aug. 2019, DOI: 10.1021/ACSAMI.9B09121/SUPPL_FILE/AM9B09121_SI_001.PDF.

[18] E. Nouri, M. R. Mohammadi, and P. Lianos, "Construction of perovskite solar cells using inorganic hole-extracting components," *ACS Omega*, vol. 3, no. 1, pp. 46–54, 2018, DOI: 10.1021/acsomega.7b01775.

[19] Y. Zhang *et al.*, "Enhancing the performance and stability of carbon-based perovskite solar cells by the cold isostatic pressing method," *RSC Adv.*, vol. 7, no. 77, pp. 48958–48961, Oct. 2017, DOI: 10.1039/C7RA07579K.

[20] H. Wei *et al.*, "Free-standing flexible carbon electrode for highly efficient hole-conductor-free perovskite solar cells," *Carbon N. Y.*, vol. 93, pp. 861–868, Nov. 2015, DOI: 10.1016/J.CARBON.2015.05.042.

[21] H. Choi *et al.*, "Cesium-doped methylammonium lead iodide perovskite light absorber for hybrid solar cells," *Nano Energy*, vol. 7, pp. 80–85, 2014, DOI: 10.1016/J.NANOEN.2014.04.017.

[22] W. Zhu *et al.*, "Communication," *Nano Energy*, vol. C, no. 19, pp. 17–26, Jan. 2016, DOI: 10.1016/J.NANOEN.2015.11.024.

[23] R. G. Niemann *et al.*, “Cs+ incorporation into CH3NH3PbI3 perovskite: substitution limit and stability enhancement,” *J. Mater. Chem. A* vol. 4, no. 45, pp. 17819–17827, Nov. 2016, DOI: 10.1039/C6TA05869H.

[24] G. Murugadoss, R. Thangamuthu, S. Vijayaraghavan, H. Kanda, and S. Ito, “Caesium −Methyl Ammonium Mixed-Cation Lead Iodide Perovskite Crystals: Analysis and Application for Perovskite Solar Cells,” *Electrochim. Acta*, vol. 257, pp. 267–280, 2017, DOI: 10.1016/j.electacta.2017.10.092.

[25] L. Atourki *et al.*, “Role of the chemical substitution on the structural and luminescence properties of the mixed halide perovskite thin MAPbI3 − xBrx (0 ≤ x ≤ 1) films,” *Appl. Surf. Sci.*, vol. 371, pp. 112–117, May 2016, DOI: 10.1016/J.APSUSC.2016.02.207.

[26] G. Niu, W. Li, J. Li, X. Liang, and L. Wang, “Enhancement of thermal stability for perovskite solar cells through cesium doping,” *RSC Adv.*, vol. 7, no. 28, pp. 17473–17479, 2017, DOI: 10.1039/c6ra28501e.

[27] Y. Fan, H. Qin, W. Ye, M. Liu, F. Huang, and D. Zhong, “Improving the stability of methylammonium lead iodide perovskite solar cells by cesium doping,” *Thin Solid Films*, vol. 667, no. March, pp. 40–47, 2018, DOI: 10.1016/j.tsf.2018.10.001.

Chapter 6

Conclusions and Recommendations

6.1 Conclusions

For the past decade, Perovskite solar cells (PSCs) have demonstrated skyrocketing efficiencies, making them suitable contenders to replace silicon-based solar cells. However, the only major drawback of the perovskites at this stage is their instability. When PSCs are exposed to moisture, light, and oxygen they can degrade instantly. Methylammonium-based PSCs are not stable because MA is a volatile material.

However, a significant enhancement in the stability is achieved when this organic cation is partially replaced with an inorganic cation like Cesium (Cs). In this MS research work, $MAPbI_3$ PSCs were single-doped with CsBr. The doping concentration of MAI: CsBr: PbI_2 (1:0:0, 0.91:0.09:1,0.85:0.15:1) were used. By doping the CsBr, the crystallinity of the film was increased with increasing the concentration and there was no prominent change in the crystal structure because the doping of the Cs was too low to introduce a new phase. The overall morphology of the film was increased because Cs are smaller in size so it enlarges the grain size. With the increase in the grain size, the grain boundaries and pinholes were reduced and overall the sites for degradation were minimized. Also, the roughness of the perovskite absorber layer was improved. Absorption spectra are enhanced at an x=0.91 doping level of the CsBr. But after this, there is a drop in the absorption spectra. When the CsBr level is increasing to x=0.09 there is an increase in the PL peak due to the reduction in the defect trap states and more electron-holes pairs are generated but after a certain doping level(x=0.15), this behavior tends to decrease.

By increasing the CsBr doping level an overall increase in the wide-bandgap (1.62eV) was observed. Usually, PSCs are fabricated following normal n-i-p device architecture, employing organic hole transport materials (PTAA, Spiro-OMeTAD, etc.) which are expensive and moisture sensitive.

On the other hand, inorganic hole transport materials are soluble in polar aprotic solvents which ultimately compromises the perovskite layer's stability and performance. To address these issues, herein, PSCs were fabricated following glass/FTO/c-TiO_2/mp-TiO_2/Perovskite/carbon paste /FTO/glass device architecture. Because carbon has a -5eV work and it is comparable with the already used electrodes (Au or Ag). It also had good conductivity and chemical stability which makes it a potential candidate for the fabrication of the PSCs at a very low cost. The water contact angle was measured on the (a) Cesium doped absorber layers and (b) Cesium doped absorber layers with carbon as a counter electrode, to check the effect of the humidity on the cesium doping and with carbon as a counter electrode. As the CsBr doping level was increased the water contact angle was increased due to the more compact film morphology. On the other hand, when the carbon was deposited on the perovskite films, they became more hydrophobic and with a more compact structure and larger contact angle to the water, the carbon/perovskite layer on top of the cell will offer better protection against moisture, and eventually, improves stability

As a result, PSCs were made by using carbon paste as a counter electrode and the best performing perovskite absorber layer (x=0.90) in the dry glove box at <10% RH. There is an increase in the Voc, Jsc, FF, and PCE by using this CsBr doped perovskite absorber material. When the CsBr doping level increases from x = 0.00 to x = 0.09, Voc increases from 0.530 to 0.659 V, Jsc from 9.56 to 18.53 mA/cm^2, and FF from 0.29 to 0.44. The resulting efficiency also increases from 1.55% for the undoped sample to 5.27% for the doped sample with x = 0.09. Also, the hydrophobic and dense carbon CE layer has a protective effect on the perovskite film by shielding it from ambient moisture. Our work proposes a new pathway for the exploration of low-cost carbon-based materials and will be potentially important for the industrial application of PSCs on a large scale.

6.2 Recommendations

1- The number of observations can be increased by preparing more samples to understand the incorporation of the CsBr in the perovskite film in a better way.

2- The elemental mapping and XPS will be performed to the exact location of the user in the perovskite film.

3- At present carbon paste, we faced many issues in achieving higher efficiency. So, Carbon electrodes can be prepared by varying the carbon and graphite ratio to understand which ratio is the most appropriate for the charge transport.

4- In this experiment, only IV characterization was performed which gives us the different electrical parameters. But the comparison of the EQE measuring will be taken to understand the exact incident electron to photoconversion efficiency.

5- A proper stability test should be performed to check the stability of the perovskite solar cells in the open environment which is the main hurdle in the commercialization of the perovskite solar cells.

6- Experiments will be carried out both in the inert environment and dry environment to check the effect of the inert and dry environment on the perovskite solar cells.

Journal Publication

Fabrication of Cs-doped Carbon-based perovskite solar cells in the ambient environment

Tanzeela Yousaf [a], Nadia Shahzad [a*], Abdul Sattar [a], Mohammad Ali Tariq[a], Naveed Hussain [a], Zuhair S. khan [a], Sofia Javed [b], Mohammad Imran Shahzad [c]

[a] U.S.-Pakistan Centre for Advanced Studies in Energy (USPCAS-E), National University of Sciences and Technology (NUST), H-12 Sector, Islamabad, Pakistan

[b] School of Chemical and Materials Engineering (SCME), National University of Sciences and Technology, H-12 Sector, 44000 Islamabad, Pakistan

[c] Nanoscience and Technology Department (NS&TD), National Centre for Physics, Islamabad, Pakistan

Abstract

The development of organometal halide-based perovskites solar cells (PSCs) has made remarkable progress in the photovoltaic technology field. The commercialization of PSCs is being rendered owing to its poor stability and higher material cost for hole transport layer (HTL) and electrodes. To counter these issues carbon-based HTL and noble-metal-free PSCs are being used. In this work, we systematically studied the effect of Cs-doping on perovskite film morphology and device performance. The results showed that when Cs-doping concentration was in the range of 9%, there was a substantial change in the optoelectronic and morphological properties of perovskite film. The grain size was improved from 70nm (undoped film) to 170nm (9% Cs-doped film) with a reduction in the grain boundaries. The device fabrication was carried out in a dry glove box at 10% relative humidity by using carbon as a counter electrode (CE). Consequently, Cs-doping with carbon CE improved the hydrophobicity and non-radiative charge recombination at the surface of the carbon/perovskite film interface. The efficiency of the devices was improved to 5.27% at a 9% Cs-doping level as compared to the 0% Cs-doping with 1.55%

efficiency. Moreover, this technique will reduce the fabrication costs of PSCs significantly promising a sustainable future for this technology.

*Corresponding Author: Nadia Shahzad (Email: nadia@uspcase.nust.edu.pk)

Keywords: Perovskite Solar Cells, Carbon counter electrode, HTL, Hydrophobic